



Optimal estimation of spectral surface reflectance in challenging atmospheres



David R. Thompson^{a,*}, K.N. Babu^b, Amy J. Braverman^a, Michael L. Eastwood^a, Robert O. Green^a, Jonathan M. Hobbs^a, Jeffrey B. Jewell^a, Bruce Kindel^c, Steven Massie^c, Manoj Mishra^b, Aloke Mathur^b, Vijay Natraj^a, Philip A. Townsend^d, Felix C. Seidel^a, Michael J. Turmon^a

^a Jet Propulsion Laboratory, California Institute of Technology, Pasadena, CA, USA

^b Space Applications Centre, Indian Space Research Organization, Ahmedabad, Gujarat, India

^c Laboratory for Atmospheric and Space Physics (LASP), University of Colorado Boulder, CO, USA

^d University of Wisconsin, Madison, WI, USA

ARTICLE INFO

Edited by Jing M. Chen

Keywords:

Imaging spectroscopy
Atmospheric correction
Remote sensing
Optimal estimation

ABSTRACT

Optimal Estimation (OE) methods can simultaneously estimate surface and atmospheric properties from remote Visible/Shortwave imaging spectroscopy. Simultaneous solutions can improve retrieval accuracy with principled uncertainty quantification for hypothesis testing. While OE has been validated under benign atmospheric conditions, future global missions will observe environments with high aerosol and water vapor loadings. This work addresses the gap with diverse scenes from NASA's Next Generation Airborne Visible Infrared Imaging Spectrometer (AVIRIS-NG) India campaign. We refine atmospheric models to represent variable aerosol optical depths and properties. We quantify retrieval accuracy and information content for both reflectance and aerosols over different surface types, comparing results to in situ and remote references. Additionally, we assess uncertainty of *maximum a posteriori* solutions using linearized estimates as well as sampling-based inversions that more completely characterize posterior uncertainties. Principled uncertainty quantification can combine multiple spacecraft data products while preventing local environmental biases in future global investigations.

1. Introduction

Remote Visible/ShortWave InfraRed (VSWIR) imaging spectrometers map spectral radiance from 380 to 2500 nm (Schaepman et al., 2009). Surface reflectance features in this interval reveal the chemistry and composition of Earth's terrestrial domains (Asner et al., 2017; Jetz et al., 2016; Ustin et al., 2004) and aquatic environments (Fichot et al., 2015; Hochberg, 2011). Recognizing this potential, authorities such as the National Academies NASA Earth Science Decadal Survey recommended new spectrometer observations with global coverage (ESAS, 2018). Meanwhile, many national space agencies are implementing orbital imaging spectrometers (Guanter et al., 2015; Iwasaki et al., 2011; Labate et al., 2009). Space missions challenge the imaging spectroscopy community to scale existing airborne campaigns into global surface property maps. At first glance a global analysis seems similar to local studies: first, calculate the calibrated radiance at the sensor; then, retrieve atmosphere properties along with surface reflectance spectra; and finally, interpret surface reflectance maps to estimate physical, chemical, or compositional properties (Thompson

et al., 2018b).

In fact, global spectroscopy is challenging because errors in reflectance estimates can become systematic biases at the global scale (Dudley et al., 2015). Elevations, biomes and latitudinal zones have distinctive surface cover but also different atmospheric properties, and both influence the measured radiance. Climatology is inadequate to constrain atmospheric interference, so retrievals must estimate it from the spectra themselves (Vermote and Kotchenova, 2008; Lyapustin et al., 2012). High water vapor loadings in the presence of aerosols and/or high solar zenith angles are particularly challenging. Aerosols create spectrally-broad perturbations that augment or attenuate radiance depending on the surface albedo, particle scattering, and particle absorption. These conditions are common in tropical environments and polluted urban areas (Dubovik et al., 2002) which are underrepresented in research on imaging spectrometer atmospheric correction. This risks a significant reduction in data yield — or worse, systematic errors in global surface property maps. Global missions will demand accurate atmospheric correction, to minimize these biases in the first place, and rigorous uncertainty predictions, so that multi-source maps can

* Corresponding author.

E-mail address: david.r.thompson@jpl.nasa.gov (D.R. Thompson).

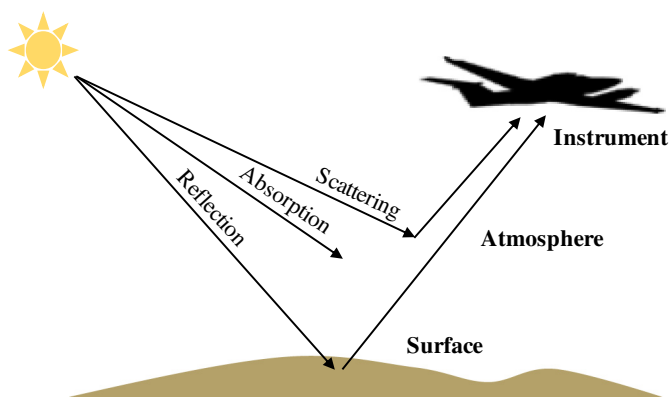


Fig. 1. Optimal Estimation is a Bayesian method to interpret remote measurements with a combined model of surface reflectance, atmosphere, and potentially instrument effects. We model the entire VSWIR spectral interval, incorporating radiative transfer physics and statistical prior information. Aircraft image courtesy NASA.

combine observations with different error profiles.

We address this challenge with *Maximum A Posteriori* (MAP) optimization of a model combining the surface, atmosphere, and instrument. Our prior research (Thompson et al., 2018c) adopts the Rodgers et al. formalism (Rodgers, 1976, 1990, 1996, 2000) known as *Optimal Estimation* (OE, Fig. 1). OE is just one of many iterative probabilistic model inversion methods, and has been used for decades by atmospheric remote sensing missions such as OCO-2 (Cressie, 2018), GOSAT (Yoshida et al., 2011), SCIAMACHY (Frankenberg and Wagner, 2005), and in future missions like MAIA (Xu et al., 2017). It finds parameters of the surface and atmosphere that are most probable given the measurement while accounting for noise and the strength of background knowledge. The approach combines measurement information with Bayesian statistical priors. Weak surface priors, which can be outweighed by measurement evidence, can resolve indeterminacy between surface and atmospheric effects without biasing surface retrievals. Prior distributions can also capture the patterns in dark vegetation or water used by traditional heuristic aerosol algorithms; such constraints already appear in the measurable statistics of Earth's surface reflectance. OE thus captures the benefits of conventional heuristic aerosol retrievals, exploiting similar properties while adding rigor and robustness. Another advantage is the ability to incorporate information distributed across the entire VSWIR spectral range without pre-selecting atmospheric retrieval windows. More recent work extends these methods to the coastal ocean domain (Thompson et al., 2019).

This existing body of work demonstrates uncertainty models consistent with the measured discrepancies between remote and in situ field data. However, recent statistical research suggests potential for further improvement (Cressie, 2018; Hobbs et al., 2017). Traditionally OE uses locally-linear approximations of the probability density based on closed-form Jacobian matrices (Rodgers, 2000). This enables fast operational MAP retrievals via gradient ascent, and a linearized prediction of posterior uncertainty. However, Cressie (2018) shows it is more statistically consistent to treat posterior uncertainties independently from the estimated state. Other recent research aims to surpass linearized uncertainties altogether. Markov Chain Monte Carlo (MCMC) samples subtler structure, including bias, local minima, and correlations in state estimates (Hobbs et al., 2017). More importantly, there is a need to test OE retrievals and uncertainties in challenging atmospheric environments with higher water vapor and aerosol loadings.

This manuscript addresses the gap with a large dataset spanning the Indian subcontinent, acquired in 2015–2016 by NASA's Airborne Visible Infrared Imaging Spectrometer, AVIRIS-NG (Thompson et al., 2018a). The data is a microcosm of global diversity with a wide range

of surface types, biomes, latitudes, elevations, and atmospheric conditions. Many scenes are tropical atmospheres with extreme aerosol and water vapor (Babu et al., 2013). We fully characterize posterior errors using MCMC sampling. We validate surface and atmosphere estimates using field instruments, and evaluate spectrum quality metrics. This illustrates the OE posterior predictive power and uncertainty for global spectroscopy of Earth's surface. Section 2 briefly reviews conventional atmospheric correction methods. Section 3 details the OE formalism, the linearized and MCMC solutions, and our specific atmospheric and surface modeling assumptions. Section 4 describes the field experiment, which includes both ground truth field sites as well as retrieval quality metrics calculated for over 20 diverse flightlines. Section 5 shows the resulting spectral information content, comparisons with references, and spectra revealing significant improvements in retrieval performance vis a vis traditional approaches. Finally, we discuss implications for future missions and avenues for future research.

2. Background

Imaging spectrometer atmospheric correction has a decades-long tradition reviewed thoroughly in Gao et al. (2009) and Thompson et al. (2018b). Historically researchers use different variants for land and water (Wang et al., 2010), and there is ongoing research into unified methods (Thompson et al., 2019). We will pass over the important category of empirical or scene-based approaches that do not easily scale for global data (Bernstein et al., 2005; Reinersman et al., 1998; Conel et al., 1987), and focus on algorithms using physics-based radiative transfer models that apply to all conditions. Here, standard practice for both land and water is a *sequential* approach that evolved from multi-band instruments. One first estimates the atmospheric state using features of the radiance spectrum, and then inverts the radiance with an algebraic function of optical parameters (e.g. atmospheric transmission and path radiance) from a precalculated lookup table. Codebases implementing this method for spectroscopy include ATREM (Gao et al., 1993), ATCOR (Richter and Schläpfer, 2002), and FLAASH (Perkins et al., 2012). Conventional methods work well for airborne investigations with clear skies and near-nadir observation geometries.

Both surface reflectance and atmospheric effects influence the radiance measurement in every channel. It is easiest to disentangle them for atmospheric terms with distinctive signatures, such as gas absorptions. However, spectrally smooth interferences such as aerosols do not have distinctive signatures apart from their influence on H₂O and surface reflectance retrievals. Multiband heuristic approaches used in the past for deriving aerosols (Guanter et al., 2008; Higurashi and Nakajima, 1999) can work inconsistently in situations with high spectral diversity. Additionally, global spectroscopic data for ecosystem observations will likely have spatial sampling near ~30 m (ESAS, 2018), too coarse to resolve cast shadows needed for dark pixel methods (Schläpfer et al., 2018). The diversity of global environments also precludes common methods relying on green vegetation (Teillet and Fedosejevs, 1995) or open-water assumptions (Wang et al., 2010). The resulting errors can thwart ecosystem trait analyses. Fig. 2 shows two examples from the AVIRIS-NG India campaign. The top panel shows a high-quality remote retrieval of vegetation reflectance. It reveals critical ecosystem traits through subtle shapes and slopes of pigment absorptions, canopy structure, and chemistry. The bottom panel is a spectrum from a city park with incorrect compensation for the local aerosol conditions. Errors in the resulting reflectance include incorrect slopes in the visible range due to uncorrected path radiance, excessive residual spikes due to H₂O vapor absorption, and loss of spectral contrast.

The resulting distortions can impact global ecosystem mapping (Thompson et al., 2018b). Fig. 3 shows global MODIS water vapor (Gao and Kaufman, 2003; King et al., 2003) and Aerosol Optical Depth, or AOD (Levy et al., 2013), as an annual average beginning in June 2017. Partitioning by land cover class (Friedl et al., 2010) reveals very

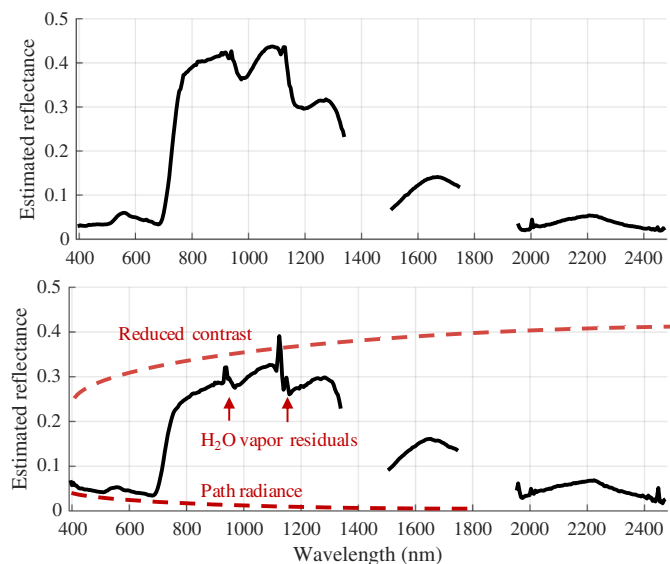


Fig. 2. Poor aerosol corrections cause distinctive distortions of vegetation spectra. The top panel shows a high-quality remote retrieval of vegetation reflectance from the AVIRIS-NG India Campaign (from scene ang20160102t072251). The bottom panel illustrates distortions induced from inaccurate compensation for atmospheric aerosol effects (from scene ang20160107t060057).

different distributions in different biomes; local environmental conditions determine the species that flourish at each region and elevation. As a consequence, errors due to atmospheric conditions will not be uniformly distributed across biomes and could distort trends in canopy traits. Examples include the combination of scattering with high aerosol loading in humid tropical environments, which can be difficult to correct accurately using an average climatology alone. Partly inundated surfaces, ice and snow, or surfaces with vegetation and other liquid absorptions, can interfere with the primary gas signatures used for H₂O estimation (Thompson et al., 2015). To the degree that existing sequential spectroscopic correction algorithms suffer from these challenges, it is because inadequate foreknowledge of surface reflectance limits the scope and accuracy of their atmospheric estimation.

Simultaneous estimation of surface and atmosphere, used already in some multi-band observations (Dubovik et al., 2011; Lyapustin et al., 2012), could address these challenges to prevent biases in maps of ecosystem functional properties and chemistry. These algorithms can represent statistical constraints on physically-plausible reflectances, optimizing surface, gas, and aerosol parameters together. A combined solution disentangles these influences by formalizing the analysts' physical intuition about features such as those in Fig. 2. Bayesian MAP model inversion algorithms such as GRASP (Dubovik et al., 2014) can predict posterior uncertainty to enable a principled fusion of data downstream from multiple times and/or observing conditions. MAP inversions were pioneered in domains with few bands (Dubovik et al., 2011), and for constrained surface types such as instrument characterization (Kuhlmann et al., 2016), aerosol retrievals (Hou et al., 2016, 2017) and tree canopies (Verhoef et al., 2017). They have recently been generalized for imaging spectrometers over more complex surfaces (Thompson et al., 2018c; Thompson et al., 2019). The next section details our implementation and some modifications to address challenging atmospheric conditions.

3. Method

Optimal Estimation (OE) models the measured radiance \mathbf{y} as a vector-valued function $\mathbf{y} = \mathbf{f}(\mathbf{x}) + \epsilon$. Here \mathbf{x} is a *state vector* of instrument, surface and atmospheric properties, $\mathbf{x} = [x_1, \dots, x_n]^T$, and ϵ is

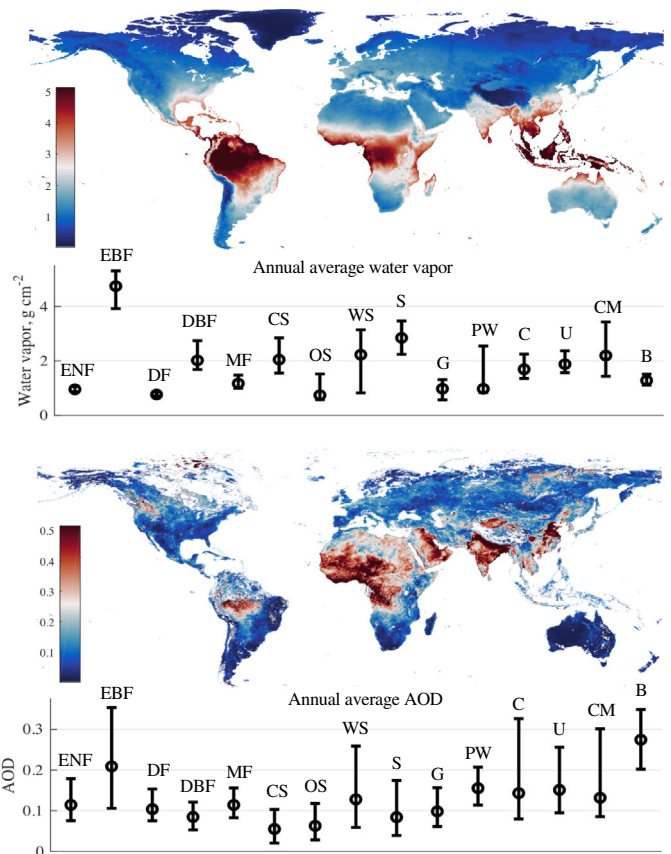


Fig. 3. Annual average MODIS AOD and water vapor estimates partitioned by land cover classification, confirming that different biomes are associated with different atmospheric environments. Error bars show the median and central half of locations for each land cover classification: Evergreen Needleleaf Forest (ENF); Evergreen Broadleaf Forest (EBF); Deciduous Forest (DF); Deciduous Broadleaf Forest (DBF); Mixed Forest (MF); Closed Shrubland (CS); Woody Shrubland (WS); Shrubland (S); Grassland/Savanna (G); Permanent Wetland (PW); Cropland (C); Urban/Built-up (U); Cropland/Natural Mosaic (CM); and Barren/Desert (B).

random observation noise (Rodgers, 2000). We refer the reader to Thompson et al. (2018c) and Thompson et al. (2019) for more detail on Optimal Estimation for imaging spectroscopy.

3.1. Single spectrum MAP estimation

The basic MAP inversion operates on a single spectrum. We decompose the posterior probability $p(\mathbf{x}|\mathbf{y})$ via Bayes' rule, with multivariate normal probability density functions:

$$p(\mathbf{x}|\mathbf{y}) = \frac{p(\mathbf{y}|\mathbf{x})p(\mathbf{x})}{p(\mathbf{y})}$$

$$\propto e^{-\frac{1}{2}(\mathbf{y}-\mathbf{f}(\mathbf{x}))^T \mathbf{S}_e^{-1}(\mathbf{y}-\mathbf{f}(\mathbf{x}))} e^{-\frac{1}{2}(\mathbf{x}-\mathbf{x}_a)^T \mathbf{S}_a^{-1}(\mathbf{x}-\mathbf{x}_a)} \quad (1)$$

Here \mathbf{x}_a and \mathbf{S}_a are the mean and covariance of a prior distribution over state vectors. \mathbf{S}_e is the observation covariance. This term includes uncertainties due to instrument noise, \mathbf{S}_y , and from unknowns in the model that are not estimated as part of \mathbf{x} . We approximate uncertainty locally in first order using \mathbf{K}_b , the Jacobian matrix of partial derivatives of unretrieved model unknowns with respect to measured radiance (Rodgers, 2000):

$$\mathbf{S}_\epsilon = \mathbf{S}_y + \mathbf{K}_b \mathbf{S}_b \mathbf{K}_b^T \quad (2)$$

The inversion initializes the state vector to the prior mean and then maximizes posterior probability by iterative gradient ascent. Each

Table 1

Notation conventions. Boldface indicates vectors, vector-valued functions, and matrices. We treat all vectors as columns for matrix algebra.

Symbol	Interpretation
$\hat{\mathbf{S}}$	Posterior covariance of state vector
\mathbf{S}_a	Covariance of state vector prior distribution
\mathbf{S}_ϵ	Covariance of random observation noise
$\hat{\mathbf{S}}$	Estimated posterior covariance at solution
\mathbf{x}	Complete state vector, $\mathbf{x} = [\mathbf{x}_{SURF}, \mathbf{x}_{ATM}]$
\mathbf{x}_a	Mean of state vector prior distribution
\mathbf{x}_{ATM}	Free parameters of atmosphere (H ₂ O and aerosols)
\mathbf{x}_{SURF}	Free parameters of surface (reflectance in each channel)
x_{H_2O}	Precipitable water vapor (cm)
x_{AOD550}	Aerosol Optical Depth at 550 nm (km)
$\hat{\mathbf{x}}$	Estimated state vector
\mathbf{y}	Radiance measurement in each channel, $\mu W \text{ nm}^{-1} \text{ cm}^{-2} \text{ sr}^{-1}$
χ^2	Cost function
σ_p	Regularization shrinkage coefficient for surface prior

iteration updates the gradients by linearizing $\mathbf{f}(\mathbf{x})$ about the current state. Since $p(\mathbf{y})$ is constant we use the objective function χ^2 :

$$\chi^2(\mathbf{x}) = \frac{1}{2}(\mathbf{y} - \mathbf{f}(\mathbf{x}))^T \mathbf{S}_\epsilon^{-1}(\mathbf{y} - \mathbf{f}(\mathbf{x})) + \frac{1}{2}(\mathbf{x} - \mathbf{x}_a)^T \mathbf{S}_a^{-1}(\mathbf{x} - \mathbf{x}_a) \quad (3)$$

Minimizing eq. 3 maximizes the log probability of the observation given the state, optimally balancing prior knowledge with measurement information. Upon convergence, first order Taylor expansion defines a posterior covariance:

$$\hat{\mathbf{S}} = (\mathbf{K}^T \mathbf{S}_\epsilon^{-1} \mathbf{K} + \mathbf{S}_a^{-1})^{-1} \quad (4)$$

where \mathbf{K} is the Jacobian matrix of partial derivatives of the measurement with respect to the state vector. Traditionally, and in previous work (Thompson et al., 2018c), \mathbf{K} is defined using the converged state vector. However, Cressie (2018) notes that this posterior uncertainty is inconsistent with its delta rule derivation. Cressie suggests estimating posterior uncertainty with a state-independent \mathbf{K} , such as one based on the prior mean \mathbf{x}_a . We will use the Cressie (2018) definition here. We calculate \mathbf{K} using analytical derivatives for surface parameters and finite difference methods for the atmospheric terms (Table 1).

Ideally the designer constructs priors and observation uncertainties using representative historical data. In practice, there is some subjectivity in parameterizing fitting these distributions. Moreover, certain investigations may intentionally compromise optimality for specific objectives. For example, a weak surface prior may produce reflectance estimates with embedded measurement noise. This may still be favorable if it preserves precise channelwise relationships for fitting radiometry correction factors or recovering band positions at tiny fractions of a percent (Thompson et al., 2018c). The diagnostic *averaging matrix* \mathbf{A} (Rodgers, 2000) can assist the designer in making these decisions and interpreting system behavior. It represents the fraction of the retrieval result attributable to the measurement rather than the prior. It is formally defined as the matrix of partial derivatives $\partial \hat{\mathbf{x}} / \partial \mathbf{x}^*$, the differential change in the estimated state vector with respect to the change in the “true” underlying state vector \mathbf{x}^* :

$$\mathbf{A} = \mathbf{S}_a \mathbf{K}^T (\mathbf{K} \mathbf{S}_a \mathbf{K}^T + \mathbf{S}_\epsilon)^{-1} \mathbf{K} \quad (5)$$

Each diagonal element of \mathbf{A} gives the *Degrees of Freedom* (DOF) for that parameter. A DOF of unity means the converged estimate is only sensitive to measurement information. A value of zero indicates that the entire result comes from the prior. The mean DOF across state vector elements is a useful scalar indicator to guide modeling decisions and evaluate the utility of alternative observing methods.

The true posterior uncertainty need not be Gaussian. Fig. 4 illustrates a non-Gaussian surface with local minima. The gradient ascent begins at the initial guess \mathbf{x}_{init} and converges to the local maximum $\hat{\mathbf{x}}$. The linearized posterior error estimate, shown here as an elliptical

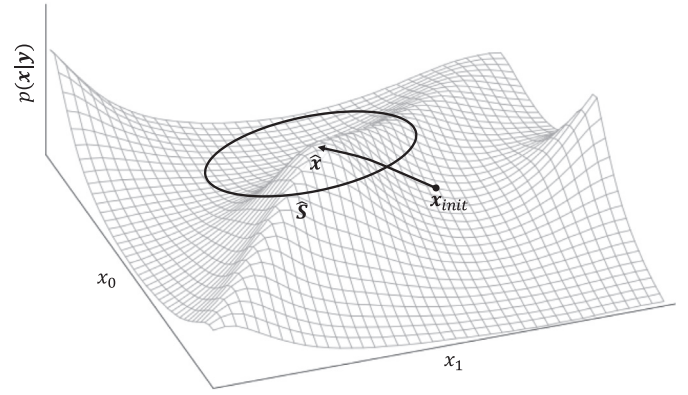


Fig. 4. The gradient ascent begins at the initial guess \mathbf{x}_{init} and converges to the local maximum $\hat{\mathbf{x}}$. The linearized posterior error estimate, shown here as an elliptical isocontour representing $\hat{\mathbf{S}}$, describes uncertainty in terms of gradients near the solution.

isocontour representing $\hat{\mathbf{S}}$, describes uncertainty near the solution. The next section uses MCMC for a more complete estimate.

3.2. Monte Carlo sampling procedure

Markov Chain Monte Carlo (MCMC) constructs a Markov Chain that matches the true posterior distribution in the limiting case of many iterations (Ripley, 1987; Gilks et al., 1996). Running the chain for many iterations samples from $p(\mathbf{x}|\mathbf{y})$, the probability of the state vector given the measurement. We use the Metropolis/Hastings method (Ripley, 1987; Gilks et al., 1996), defining a function $g(\mathbf{x})$ proportional to the desired probability density. Eq. 1 yields:

$$g(\mathbf{x}) = e^{-(\mathbf{y}-\mathbf{f}(\mathbf{x}))^T \mathbf{S}_\epsilon^{-1}(\mathbf{y}-\mathbf{f}(\mathbf{x}))} e^{-(\mathbf{x}-\mathbf{x}_a)^T \mathbf{S}_a^{-1}(\mathbf{x}-\mathbf{x}_a)} \quad (6)$$

The posterior density fills a tiny fraction of the high dimensional state space, so we initialize the Markov Chain using a random draw \mathbf{x}_0 from the OE MAP posterior uncertainty. This begins the sampling in the proper neighborhood while permitting discovery of alternative minima. Each subsequent iteration t draws a candidate sample \mathbf{x}' from a *proposal distribution* centered on the current state \mathbf{x}_t , with a covariance based on the linearized uncertainty prediction $\hat{\mathbf{S}}$. Denoting a multivariate Gaussian distribution with mean μ and covariance matrix Σ as $\mathcal{N}(\mu, \Sigma)$, we draw:

$$\mathbf{x}' \sim k \mathcal{N}(\mathbf{x}_t, \hat{\mathbf{S}}) \quad (7)$$

Following community practice and theory we use a scaling factor k of 0.02 to achieve an efficient acceptance rate of 25–50% (Bedard, 2008). The Metropolis Hastings criterion draws a uniform random number $I \in (0, 1)$, accepting the candidate when:

$$I < \min(q, 1) \text{ for } q = g(\mathbf{x}')/g(\mathbf{x}_t) \quad (8)$$

If the candidate is accepted, $\mathbf{x}_{t+1} = \mathbf{x}'$. Otherwise, $\mathbf{x}_{t+1} = \mathbf{x}_t$. We set the posterior density to zero outside the range of the atmospheric lookup table, but we do not bound surface terms because slight negative reflectances can still produce well-defined radiance values. Extremely dark channels commonly dip below zero due to natural noise fluctuations. We draw 20,000 samples in each of the simulations described below, with periodic random restarts every 2000 iterations and a “burn-in period” of 200 iterations (Gelman et al., 2011) following every re-initialization. This ensures that the samples explore the entire solution space. Collectively, the samples estimate the posterior uncertainty while respecting any locally-nonlinear response of the forward model.

3.3. Atmospheric and surface models

Optimal Estimation predicts measured radiances with a “forward

model” of the instrument, atmosphere, and the surface. In principle the retrieval can estimate any forward model parameter. Our state vector is similar to Thompson et al. (2018c) with surface parameters \mathbf{x}_{SURF} and atmospheric parameters \mathbf{x}_{ATM} . We estimate instrument noise using a comprehensive physics-based model of the instrument optical, detector, and electronic efficiency (Thompson et al., 2018c). The noise is channel- and signal-dependent, and recalculated for each spectrum.

The surface state $\mathbf{x}_{SURF} \in \mathbb{R}^{425}$ has a separate reflectance value for each of AVIRIS-NG's 425 instrument channels. Following Thompson et al. (2018c), our surface prior is a collection of multivariate Gaussian components. We begin by fitting 8–10 components to a diverse library of surface reflectances that collectively describe features of physically plausible spectra. K-means clustering specifies the component centers, and Expectation Maximization (EM) fits the covariances. Unlike prior work, we form additional components using random geographic mixtures (Keshava and Mustard, 2002) drawn from the endmember spectra in the library. This helps the system model intermediate cases of fractional cover by multiple materials. In all cases, heavy numerical regularization (Theiler, 2012) further broadens these distributions so that they can fit spectral features which do not occur in the library. Specifically, we use a shrinkage term σ_p that scales the covariance matrix diagonal, interpolating between the original covariance \mathbf{S} and the identity matrix \mathbf{I} according to $(1 - \sigma_p)\mathbf{S} + \sigma_p\mathbf{I}$. We typically use small values such as $\eta = 10^{-6}$ within key atmospheric features, promoting smoothness in (for example) water absorption bands, and larger values elsewhere. The resulting prior is intentionally weak, preventing non-physical step discontinuities without biasing the retrieved reflectance features. Several regions are particularly useful for atmospheric estimation: the UV range from 300 to 400 nm, which provides important aerosol information; and the near-infrared range from 900 to 1200 nm that includes water vapor atmospheric absorption features. We hypothesize a sufficiently sensitive instrument might draw additional aerosol information from distortion of these near-infrared water absorption features. We use the Euclidean-nearest component distance as the prior.

Our atmospheric model also builds on Thompson et al. (2018c). We first translate the observed radiance spectrum $\ell_{obs} = [\ell_{\lambda 1}, \dots, \ell_{\lambda m}]^T$ into a top of atmosphere reflectance ρ_{obs} which normalizes for the incoming solar illumination using the zenith extraterrestrial solar downward irradiance e_o , and a factor ϕ_o representing the cosine of the solar zenith angle. We adopt a convenient Lambertian decomposition of ρ_{obs} :

$$\rho_{obs} = \frac{\ell_{obs}\pi}{\phi_o e_o} = \rho_a + \frac{\mathbf{t} \cdot \mathbf{x}_{SURF}}{1 - (\mathbf{s} \cdot \mathbf{x}_{SURF})} \quad (9)$$

with the \cdot symbol signifying element-wise multiplication. The path reflectance is ρ_a , the spherical sky albedo is \mathbf{s} , and \mathbf{t} represents the atmospheric diffuse and direct transmittance. The surface reflectance itself is the surface state ρ_{SURF} . We calculate these terms for a grid of atmospheric state values using the RTM and cache them in a lookup table. Given a candidate atmospheric state, we perform multilinear interpolation within this table to set the remaining terms of Eq. 9. We determine atmospheric parameters using conventional band ratio methods described in Thompson et al. (2018c), and then initialize surface reflectance by algebraic inversion. The atmospheric state \mathbf{x}_{ATM} contains the total water vapor column x_{H_2O} in $g\ cm^{-2}$, and three scalar values describing the extinction due to different types of atmospheric boundary layer aerosols. The three options are not intended as actual species classifications, but rather as representative optical properties that span the space of likely distortions.

We include three aerosols in our simulations: Type A, derived from soot properties; Type B, from dust; and Type C, based on sulfate particles. These choices represent distinct aerosol microphysical and optical properties (Table A.6). Soot is highly absorbing, dust is moderately absorbing, and sulfate, which uses a relative humidity of 70%, is strongly scattering. In terms of particle size, these choices range from small (soot) to moderate (sulfate, $\sim 0.1\ \mu\text{m}$) and large (dust, $\sim 1\ \mu\text{m}$).

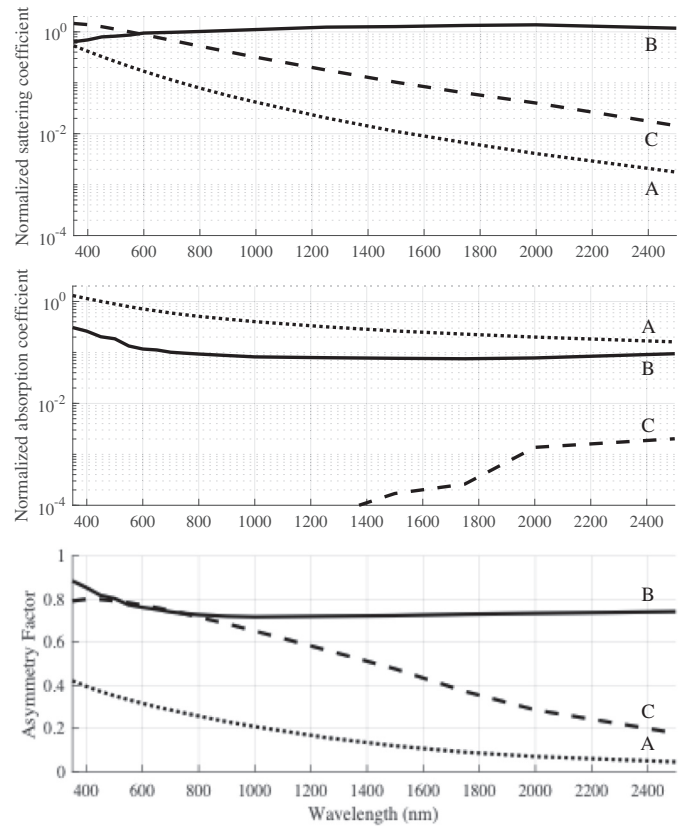


Fig. 5. The aerosol signatures used in the retrieval are based on three particle types which typify different absorption and scattering efficiencies. Top panel: Aerosol absorption coefficient for types A, B, and C. Middle panel: aerosol scattering efficiency. Bottom panel: aerosol scattering asymmetry factor. All efficiencies are normalized to unity at 550 nm. Combinations of these yield a wide range of different scattering and absorption spectra to correct varied particle types and vertical distributions.

Soot and sulfate are spherical particles, while dust is nonspherical. Our choices therefore enable a variety of spectral extinctions (through the Angstrom exponent, which is primarily a measure of particle size), single scattering albedos (SSAs, characterized by imaginary part of refractive index in addition to size), and phase functions (including sphericity in addition to size and refractive index). Mixing these produces scattering and absorption for diverse particle types and vertical profiles, acting as a structured error term to improve reflectance fidelity.

Our state vector represents the total aerosol effect with the aerosol optical depth at 550 nm for each signature: τ_A , τ_B , and τ_C . Fig. 5 shows the scattering coefficients, absorption coefficients, and asymmetry parameters, written b_{sca} , b_{abs} , and a respectively (Lin et al., 1973). We normalize them so that the combined total extinction is unity at 550 nm, and the product with AOD values at 550 nm forms the spectrally-defined scattering and absorption coefficients. We also parameterize aerosol scattering phase functions with an asymmetry parameter formed by the weighted average of the three signatures.

In summary, we define four atmospheric state variables: water vapor, and optical thickness parameters for each aerosol profile, producing a state vector with 429 elements. We set the H_2O vapor prior to be broad and uninformed. We give each aerosol type a climatological prior appropriate for its region, as determined by nearby AERONET data. Specifically, we divided the continent into climatological latitude and longitude areas and accumulated means and standard deviations of AOD and SSA from AERONET observations during the campaign. Appendix A provides additional detail on the procedure. This was a general purpose compromise and regional studies might use even more

specific climatologies such as those of Babu et al. (2013). One could also seed priors using coincident measurements from orbital data. We calculate coefficients for the lookup table using the MODTRAN 6.0 Radiative Transfer Model (Berk et al., 2014). We assume they are homogeneously distributed within the bottom 3 km of the atmospheric column; extreme deviations might favor other assumptions.

4. Experimental approach

Our field validation experiments compared OE performance with conventional methods, evaluating predictive uncertainty with both linearized and Monte Carlo estimation. We analyzed the 2015–2016 segment of an AVIRIS-NG campaign in India. This campaign was a collaboration between the National Aeronautics and Space Administration (NASA) and the Indian Space Research Organization (ISRO) (Thompson et al., 2018a). The AVIRIS-NG airborne imaging spectrometer flew onboard an ISRO King Air B-200 aircraft acquiring downward-looking spectral radiance cubes from 380 to 2500 nm at 5 nm spectral resolution. The aircraft visited sites across the sub-continent over several seasons; at the time of this writing it may be the most geographically diverse airborne imaging spectrometer campaign yet conducted. Acquisitions showed a range of atmospheric conditions from polluted urban skies to clear Himalayan conditions; they included elevations from sea level to 6 km and latitudes ranging from the tropics to mid latitudes. Scene content consisted of natural biomes including forests, wetland estuaries, barren desert, grassland, glaciers and bare geology. There were many examples of developed areas with urban environments, agriculture, and the wildland interface.

Our first experiment validated the inversion algorithm using in-situ data at selected sites (Table 2). Site Des-I was a calibration/validation exercise at Desalpar playa, a bright uniform soil surface with a stable reflectance (Fig. 6). AVIRIS-NG overflew the site at an altitude of 5 km providing approximately 5 m ground sampling distance. Coincidentally with the overflight, a field team acquired surface reflectance measurements with handheld Analytical Spectral Devices, Inc. (ASD) field spectroradiometers. The team traversed a grid pattern acquiring data and periodically returning to a leveled reference panel against which the target radiances were ratioed to calculate an area-average surface reflectance. Previous work evaluates this acquisition using conventional atmospheric modeling strategies (Babu et al., 2019), validating the field data and the efficacy of MODTRAN 6.0 *vis a vis* vector codes like 6S.

Sites Kar-I, Kar-II, and Kar-III were soil and vegetation spectra from the Karnataka region, a rural area near a large national forest. This was a contrasting surface with more vegetation. The AVIRIS-NG spatial sampling was approximately 5 m. A ground team visited several agricultural fields in the flightline, measuring atmospheric aerosol optical depth with Microtops-2 sunphotometers as well as plant canopy reflectance. We did not expect the reflectances to match AVIRIS-NG directly, since the fields were not uniform and the in situ data showed variable canopy density and condition. The AVIRIS-NG sampling of 5 m

Table 2

Performance of three different retrieval methods for the in situ validation experiments: Standard atmospheric correction using heuristic sequential surface/atm retrievals (S), Optimal Estimation using a stock rural aerosol model (OE-R), and Optimal Estimation with the mixture of three canonical aerosol optical types (OE).

Site	$\hat{\rho}_s$ Spectral Angle			$\hat{\rho}_s$ RMSE		
	S	OE-R	OE	S	OE-R	OE
Kar-I:	0.054	0.049	0.045	0.007	0.006	0.006
Kar-II:	0.030	0.025	0.024	0.006	0.005	0.005
Kar-III:	0.028	0.019	0.018	0.006	0.004	0.004
Des-I:	0.046	0.037	0.039	0.019	0.016	0.022

Boldface signifies the best performance.



Fig. 6. Desalpar Playa, Gujarat Province, India. A spectralon panel, leveling tripod, and a tarp target used for localization are visible in the background.

included the soil around each plant, a situation typically addressed with linear areal models (Keshava and Mustard, 2002). Standard practice uses Multiple Endmember Spectral Unmixing (MESMA), a linear model comprised of a small set of one to three endmembers together with photometric shade in proportion to the areal coverage of each (Roberts et al., 1998). The most common general purpose model uses soil, non-photosynthetic vegetation, and green vegetation endmembers (Dennison and Roberts, 2003). To upscale the in situ data, we formed a surface reflectance library with selected examples of soil and non-photosynthetic vegetation from community-standard historical datasets (Serbin et al., 2018; Elvidge, 1990). We also appended the in situ spectra from the field experiment. We then formed field-average remote spectra from a rectangular area of about 400 m² around the sample sites, and then matched these with nonnegative weighted combinations of library endmember spectra. Fits by a nonnegative least squares solver (Lawson and Hanson, 1995) produced just a few nonzero weighting coefficients, indicating that the spectra were well-described by a linear combination of the three classes. Fig. 7 shows the components and model result for the Karnataka III site. Note that we only used this linear

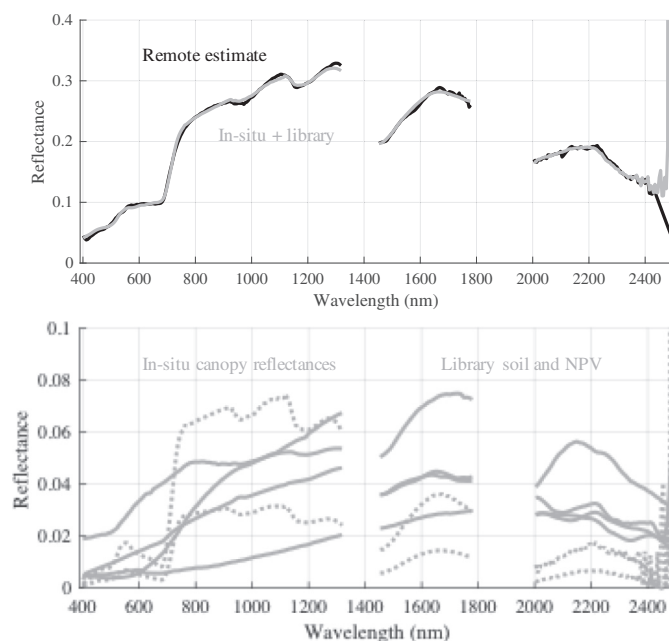


Fig. 7. Top: Karnataka site II showing the remote reflectance estimate and model based on in situ spectra. Bottom: mixture model component spectra, scaled by their optimal weighting coefficients. The dotted lines indicate vegetation spectra from canopies measured in situ. The solid lines indicate historical spectra from libraries of soil and Non Photosynthetic Vegetation (NPV).

mixture to upscale the field reflectance at 5 m resolution for comparison with the remote measurement. In contrast, the airborne retrieval always represented the surface with regularized multivariate Gaussians.

We calibrated the AVIRIS-NG data to radiance units while correcting for electronic effects and spectral response tails (Zong et al., 2006; Thompson et al., 2018a). We then produced georectified data cubes and ascribed geographic coordinates following standard practice. Finally, we performed MAP and MCMC estimation with each remote spectrum. For all three validation sites, we compared OE performance to the standard AVIRIS-NG atmospheric correction (Gao et al., 1993; Thompson et al., 2015), a sequential retrieval of atmosphere and surface. It estimated H₂O vapor using the top of atmosphere reflectance profile in several narrow absorption features. It did not estimate aerosol parameters, but instead relied on a rural aerosol model with 50 km visibility. This default was a compromise for large-scale production products, and formed the official reflectance data from the India campaign. The standard algorithm used multiplicative factors to reduce systematic residual errors from instrument sampling and radiative transfer uncertainties (Thompson et al., 2015). Following long-standing practice for airborne instruments such as AVIRIS-C and AVIRIS-NG, we had calculated these channelwise correction coefficients vicariously in advance from a spectrally smooth target imaged early in the campaign. We held them near unity to avoid altering absolute radiometry. We compared retrieval accuracy with in-situ data using the spectral angle and Root Mean Squared Error (RMSE). We also compare the predicted posterior confidence to the realized error, budgeting two independent 1% uncertainties to the in-situ data to account for both the spectrometer calibration and spectralon reflectance BRDF.

Next we compared the algorithms' performance on a multi-site set of over 20 distinct scenes surveyed by the campaign, analyzing rectangular regions with approximately 18,000 distinct spectra per scene and inverting atmospheric parameters independently for each spectrum. Fig. 8 shows typical flightlines from the first two flight days, with dense urban areas, partly vegetated cropland mosaics, and the wildland interface. Aircraft altitudes of 4–8 km produced 4–8 m Ground Sampling Distances (GSDs). Many flightlines showed moderate atmospheric aerosol and water vapor loading, with estimated AODs exceeding 0.5 and water vapor at or above 3.0 g cm⁻².

We calculated several retrieval quality metrics. The score q from Thompson et al. (2018a) measured reflectance roughness in the absorption band at 1140 nm to diagnose aerosol or surface interference with the water vapor correction (Guanter et al., 2008; Gao and Goetz, 1990). It is the difference between the estimated reflectance with and without smoothing by a 5-channel moving average, accounting for the noise contribution σ_{REF} using a reference interval outside the absorption feature:



Fig. 8. Example flightline segments from the India campaign. The top three panels show Dec. 18, 2015 segments with dense urban cover (Kalaburagi, Telangana Province, top panel), the wilderness interface (top middle panel), and cropland (bottom middle panel). The bottom panel shows a typical wilderness segment from the following flight day.

$$\sigma_{H_2O} = \sqrt{\frac{\sum_{\lambda} (\rho_s(\lambda) - \hat{\rho}_s(\lambda))^2}{n_{H_2O}}}, \sigma_{REF} = \sqrt{\frac{\sum_{\lambda} (\rho_s(\lambda) - \hat{\rho}_s(\lambda))^2}{n_{REF}}} \quad (10)$$

where ρ_s was the smoothed reflectance, the H₂O summation spanned 1087 to 1162 nm with n_{H_2O} channels, and the reference region spanned 1002 to 1077 nm with n_{REF} channels. This permitted a noise-invariant error metric $q(\mathbf{x})$:

$$q(\rho_s) = \sqrt{\sigma_{H_2O}^2 - \sigma_{REF}^2} \quad (11)$$

A second performance score quantified surface-induced biases in the H₂O column retrieval. Surface materials with overlapping absorption features could disrupt vapor absorptions and consequently the retrieved amount. One such interfering feature was liquid water in vegetation, which occasionally survived the compensatory algorithms described in Thompson et al. (2015). We fit a simple linear relationship mapping the surface albedo and NDVI to the H₂O prediction and used the H₂O variance explained as an additional performance score. A third performance statistic was the total standard deviation of the H₂O vapor retrieval. Since we intentionally limited this study to small subscenes, the water vapor column was expected to be nearly constant favoring smaller standard deviations. Finally, we compared the retrieved AOD550 to MODIS Terra observations acquired from the same day, averaging MODIS MOD04 AOD550 retrievals within a one degree latitude grid square around the flight. There was no exact spatiotemporal coincidence so we expected some divergence. However, the approximate MODIS alignment was an independent check on broader-scale regional trends.

Multi-spectrum AOD calculations should consider the different surfaces in the scene and the varied information provided by each. Fig. 9 shows an example of retrieval variability for a scene with diverse surface materials. The top panel shows AVIRIS-NG data in visible wavelengths, revealing regions of dark green vegetation as well as bare soil annotated by (a) and (b) symbols respectively. The dark green vegetation lies in a region of the surface probability distribution with stronger spectral constraints (particularly on short wavelengths). Consequently, these retrievals are expected to be more accurate. The middle panel shows the AOD550 retrieval, which depends somewhat on the surfaces; AODs over bare areas are less extreme thanks to influence by the prior. This is consistent with the bottom panel showing high marginal predicted AOD550 uncertainty in the bare soil areas. To determine the best prediction for the whole scene, we simply average the predictions of the most confident 5% of spectra. This is a simple approach; a more sophisticated and accurate solution might infer a smooth atmospheric field from all spectra (Thompson et al., 2018c).

5. Results

We first illustrate the spectroscopic cues influencing retrieved atmosphere and surface values. Averaging kernels (i.e. rows of the A

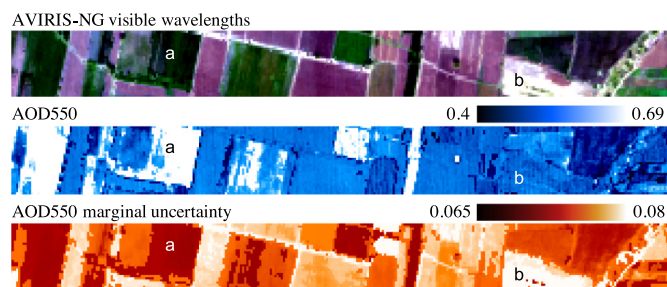


Fig. 9. Example of retrieval variability for a scene with diverse surface materials. Top: AVIRIS-NG visible wavelengths, showing regions of dark green vegetation (a) as well as bare soil (b). Middle: AOD550 retrieval, which varies slightly due to the different constraints resulting from the surfaces. Bottom: posterior uncertainty predictions. See text for explanation.

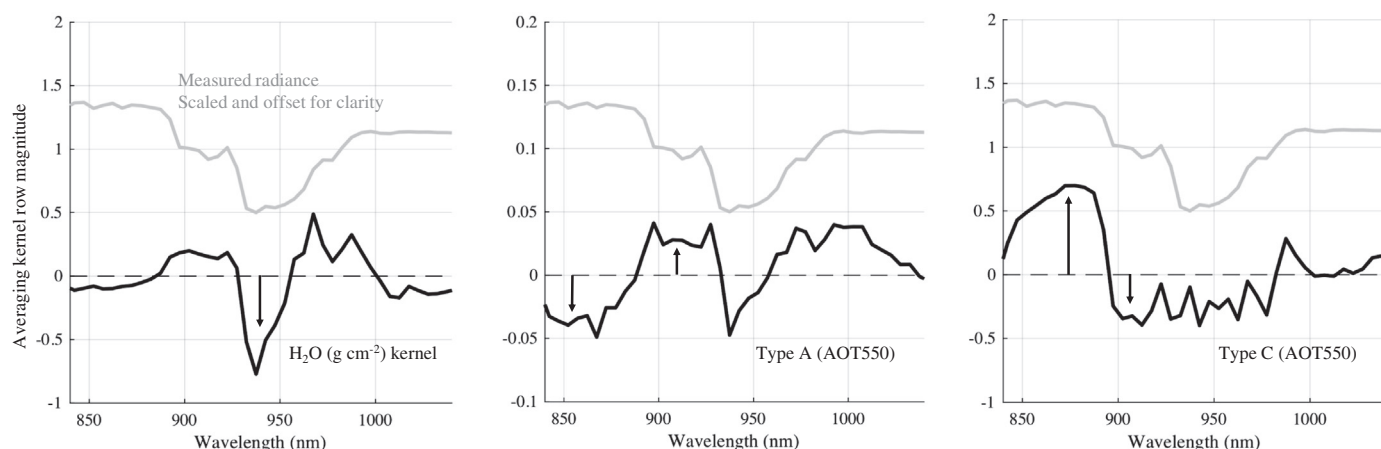


Fig. 10. Atmospheric state vector responses to the H₂O absorption feature at validation site III. Three panels plot rows of the A matrix (i.e. averaging kernels) that indicate how each state vector element responds to the measured radiance (in grey, for reference). Left panel: averaging kernel for column H₂O, which matches the shape of the absorption feature. Middle panel: AOD for Aerosol type A (derived from soot, with a lower SSA). Right panel: Aerosol type C (derived from sulfate, with a high SSA). See text for interpretations.

matrix) indicate appropriate spectroscopic features associated with the atmospheric elements of the state vector. To review, the A matrix shows the estimates' sensitivities to changes in the true state. The India campaign averaging kernels suggest all atmospheric parameters can get some information from the shapes of water vapor absorptions. Fig. 10 shows three representative kernels near the 940 nm H₂O vapor absorption, calculated at the solution state for site Kar-III. The left panel shows the averaging kernel for the H₂O parameter. An arrow indicates that this state element responds to a deeper H₂O absorption. The middle panel shows AOD for Aerosol type A, which is derived from soot and has a low SSA. Here a narrow, deep H₂O feature combined with a lower continuum indicates high AOD, since together they suggest a uniform attenuation due to aerosol absorption. The right panel shows spectroscopic features indicating high AOD for Aerosol type C, which is derived from sulfate and has a high SSA. Here, a high continuum and a broad, shallow H₂O feature suggest a uniform additive path radiance effect that reduces the fraction of photons reaching the low dense layers of tropospheric water vapor. We note again that aerosol vertical distributions were presumed uniform within a 3 km thick layer. Other vertical distributions might produce the same spectrum perturbations with different aerosol types and optical depths; however, they would be corrected using the restricted palette of signatures available to the inversion. For this reason and others, we caution against interpreting retrieval outcomes as aerosol particle properties.

Fig. 11 compares AOD₅₅₀ measurements by in-situ sensors to the remote total AOD₅₅₀. The error bars show predicted standard deviations. In the AVIRIS-NG case, these predictions come from the marginal AOD₅₅₀ uncertainties combined in quadrature. We derive uncertainty of the in situ sensor based on the sequence of acquisitions acquired within 1 h of the flightline start. We find the in situ and remote methods to be broadly consistent; the correlation coefficient $r = 0.83$ implies a good match, and the values align to within expected errors.

The averaging kernels show how atmospheric parameters respond to different perturbations of the reflectance continuum. This compensatory change can come either from reflectance or atmosphere, to a degree determined by the balance of measurement and prior information. Specifically, it depends on the observation uncertainty (a combination of calibration unknowns and measurement noise) versus the strength of the prior distribution. Fig. 12 illustrates this relationship for the Desalpar (Site Des-I) spectrum. The contour plot shows the mean spectral reflectance DOF for different sensor SNR assumptions and regularization choices. For clarity, we plot the regularization term as a standard deviation, i.e. $\sigma_p = \sqrt{\eta}$. Contours show the mean Degrees of Freedom (DOF) for the reflectance parameters for various values. We

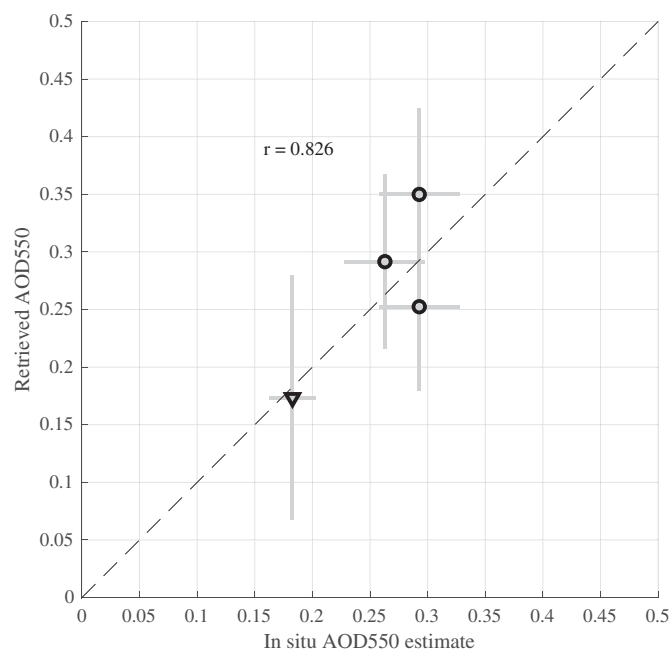


Fig. 11. Remote and in situ AOD₅₅₀ estimates. Error bars show 1σ predicted uncertainties. The correlation coefficient is $r = 0.826$.

have simplified this illustration for clarity; in the actual retrievals, both SNR and the prior are spectrally-valued quantities with rich correlations and covariance structures under full control of the designer. Also note that, while SNR is defined by first principles in our experiments, there is still some subjectivity in the budget for radiometric calibration unknowns at the sub-percent level. These act as random variables adding a small amount of additional noise. The main control on the strength of the surface prior is the parameter η . Conditions that would favor the prior include small values of η , or low-SNR observations. Fig. 13 panels A and B show the converged estimate for low- and high-DOF cases.

The Maximum A Posteriori solutions for validation sites align well with the MCMC estimates. Fig. 14 shows reflectance terms of the state vector, with the OE result in black showing linearized error estimates as 1σ error bars. The MCMC samples from the posterior reflectance distribution appear in red. Reassuringly, the MAP and MCMC estimates align closely with the in situ model, suggesting that the linearized error

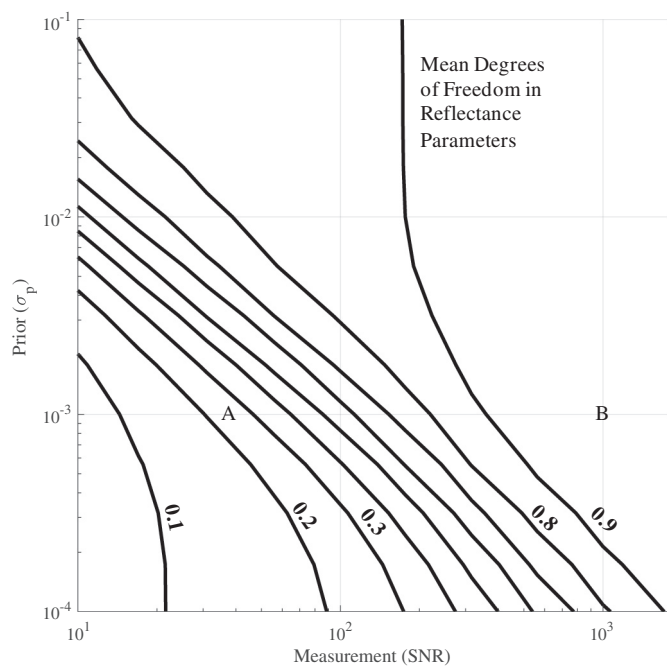


Fig. 12. Mean Degrees of Freedom (DOF) for the reflectance parameters, for the Desalpar spectrum, for various values of assumed Signal to Noise (SNR) and σ_p . A and B show representative cases of low- and high-DOF retrievals. Two specific alternatives noted A and B appear in Fig. 13.

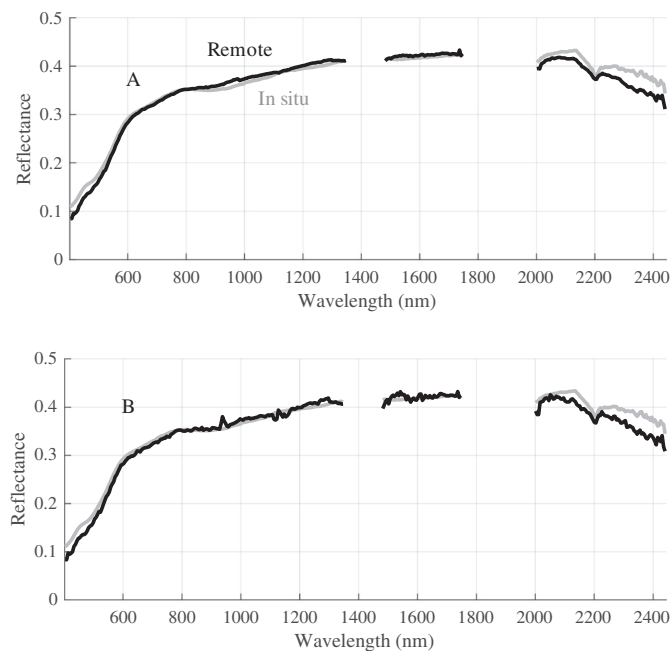


Fig. 13. Low- and High-DOF retrievals from the cases illustrated in Fig. 12.

estimate is a faithful representation of the true posterior error in surface reflectance near the solution. This is not surprising, because radiance is mostly linear with respect to small changes in surface reflectance.

Fig. 15 compares atmospheric parameters, where more nonlinear relationships induce a small divergence between the two solutions. The with the total combined aerosol optical depth on the horizontal axis and the H_2O vapor column estimate on the vertical axis. The black error bars show 1σ uncertainty, with OE estimates in black and MCMC posterior samples in red. A dashed line indicates the combined in situ sunphotometer measurement at the time of the overflight, with 1σ as a

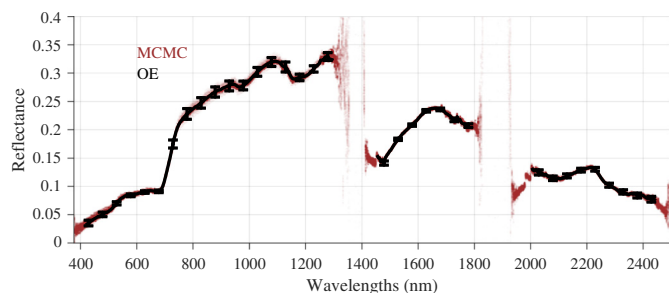


Fig. 14. Typical OE and MCMC result for surface reflectance.

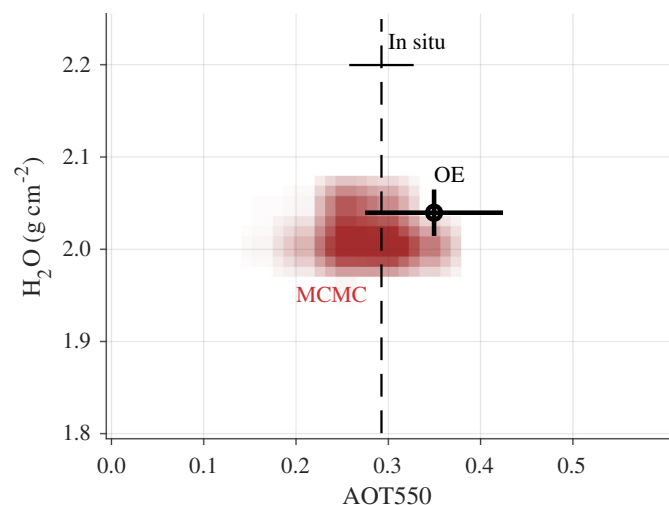


Fig. 15. Typical OE and MCMC result for atmospheric AOD550 and H_2O vapor column abundance.

crossbar. The OE retrieval overestimates AOD550 in this flightline. This is unlikely to be caused by the presence of multiple local minima (the MCMC samples do not appear multimodal), but could be due to influence from the prior mean or by nonlinearity not captured by the multilinear lookup table or the iterative MAP retrieval. Regardless, the in situ measurement and MCMC solution lie within the posterior standard deviations, so both remote estimation methods are statistically consistent with each other and with the in situ measurements.

Performance metrics are best for Optimal Estimation with the three parameter aerosol representation. Fig. 16 shows the residual reflectances for each validation site, i.e. the difference against the models calculated from in-situ data and the remote retrieval. Most residuals are $< 2\%$ in absolute reflectance units. However, the conventional retrieval has residual “spikes” in water vapor bands and some departures near deep absorption features. The OE case significantly improves these artifacts. This is consistent with prior findings from Thompson et al. (2018c) though in this case we compare OE to an alternative correction code that differs in both the inversion approach (sequential and algebraic vs. Bayesian MAP) and the core Radiative Transfer model (6S vs. MODTRAN 6.0). It is possible that differences in radiative transfer calculations also contribute to the improvement in spectrum residuals. Shaded areas represent 50% and 95% posterior uncertainty intervals on the residual for the three-component OE model. Those residuals, represented by the black lines, are broadly consistent with the predicted confidences. Table 2 compares spectral angle and RMSE scores for the standard method, OE using both a classic rural aerosol model (only retrieving the total AOD550), and the three parameter aerosol model (with AOD550 retrieved independently for each of the components). Bold entries indicate the best scores.

Finally, Table 3 reports performance for the multi-flightline validation experiment. Columns indicate spectrum quality metrics q , the

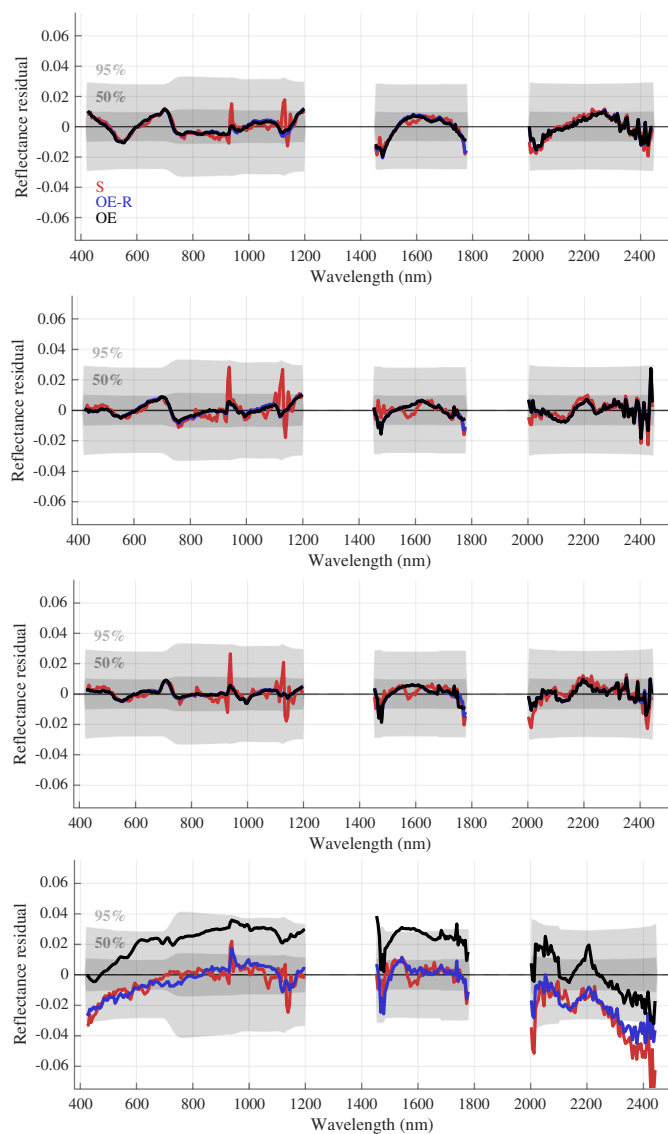


Fig. 16. Spectral reflectance residuals vs. models based on in situ data. From top to bottom: Kar-I, Kar-II, Kar-III, and Des-III. Shaded regions show 50% and 95% posterior predicted uncertainty envelopes.

standard deviation of H_2O estimates, and the fraction of variance explained by surface reflectance properties (NDVI). The best scores appear in boldface. The OE approach significantly outperforms, improving spectrum quality metrics by factors of 2–10. The average overall improvement is 81.4%. Additionally, OE significantly reduces the variance of column water vapor estimates. There is less improvement in the fraction of that variance explained by surface properties. This is because, as noted previously, different surface types provide different constraints on aerosols, and the AOD550 affects the level of water vapor required to explain those absorption features. Insofar as the OE approach provides more accurate aerosol estimates than the fixed assumptions used in the standard algorithm, it also enables better retrievals of column water vapor.

Fig. 17 relates the retrieved AOD550 values from AVIRIS-NGs to those of the MODIS Terra MOD04 Aerosol product, with error bars representing the standard deviations over flightlines and $1^\circ \times 1^\circ$ grid squares, respectively. All the measurements are consistent to within the spatiotemporal variability. The correlation coefficient $r = 0.835$ implies that the airborne measurement explains 70% of the MODIS variance.

The diverse India dataset also shows how OE can improve

atmospheric distortions under the more challenging conditions. Fig. 18 shows the relative (normalized) aerosol optical depths of the signatures in two such scenes. The panel at left favors the type C aerosol profile, which has a higher overall SSA than the other types. The spectrum directly below shows a vegetation example from the scene, the point having the highest estimated Normalized Difference Vegetation Index (NDVI). We show the retrieval result from both standard and OE approaches. The column at right shows a similar comparison for an urban scene that favors a higher fraction of aerosol type A, a signature derived from soot particles with a lower SSA. The interference effects, such as the shape of water vapor residuals and the distortion of the Visible-Near Infrared vegetation reflectance profile near 400 nm, differ for the two aerosol types. This fact, the overall improvement in residuals using OE, and the consistent retrieval of a similar aerosol optical type from the different spectra in each scene are all consistent with the claims that (1) there is aerosol information in the spectroscopic data beyond total AOD, and (2) our retrieval methodology is sensitive to these effects. The experiments suggest that many reflectance errors in the standard approach are related to aerosol loading, and that the optimal estimation retrieval improves these errors.

6. Discussion and conclusions

The India experiments yield several key outcomes. First, they show that linearized posterior uncertainties (Cressie, 2018) generally agree with MCMC estimates. They correspond best for surface terms, consistent with Eq. 9 where the measured signal is nearly linear in surface reflectance. Uncertainties also agree well for water vapor that draws information from unsaturated absorption bands where the transmission is approximately linear with respect to concentration (Thompson et al., 2015) and thence with the measurement. Aerosols are more complicated, exerting various wavelength-dependent attenuating and additive effects. Not surprisingly, the linearized AOD uncertainty predictions depart more significantly from the MCMC posterior.

Second, aerosol retrievals exploit subtle differences in the shape and depth of atmospheric absorption features. This contrasts with conventional heuristics (such as the dark green vegetation method) that rely on more visually-obvious patterns. It underscores the benefits of full-spectrum OE approaches for improving reflectance accuracy. Exploiting the features for AOD estimation requires high accuracy in the underlying radiance. Small departures from the nominal spectral response function due to spatial nonuniformity, internal scatter, or other stray light effects, can artificially broaden atmospheric absorptions and distort the information present in these high-contrast signatures (Thompson et al., 2018a). While AVIRIS-NG benefits from significant attention to - and correction for - these effects, our tests suggest that high-fidelity instrument design, radiance calibration, and reflectance retrievals must all improve in concert to continue advancing atmospheric retrievals.

Informed priors are a natural way to fine-tune the inversions. We find the system is generally unimodal, so poor prior assumptions generally degrade performance gracefully by biasing retrieval results without inducing catastrophic local optima. Here our reflectance priors are intentionally under-constrained with regularization to represent diverse surface spectra. We constrained surface distributions just enough in key atmospheric intervals so that the implied spectral continuity would reveal information about the atmosphere, attributing (for example) sharp H_2O absorption signatures to the atmosphere rather than the surface. Alternative “reflectance basemap” methods offer stronger surface constraints for high numerical leverage on atmospheric parameters.

There are several compelling directions for future investigations. Further study could refine aerosol retrievals to extract and validate useful atmospheric products. Here we treat aerosol contributions only as structured error terms in the service of reflectance accuracy. This is effective for surface studies but we cannot yet interpret the atmospheric

Table 3

Performance metrics for standard atmospheric correction (S) and OE surface/atmosphere estimation (OE) in the multiple-flightline test. Columns indicate spectrum quality metrics q , the standard deviation of H₂O estimates, and the variance explained by surface reflectance properties (NDVI and mean reflectance magnitude) for both approaches. The best scores appear in boldface.

Flightline	Content	H ₂ O		Residual magnitudes ($q \times 100$)			H ₂ O Divergence (σ)		NDVI Correlation	
		g cm ⁻²	AOD ₅₅₀	S	OE	Improvment.	S	OE	S	OE
ang20151218t104206	Urban	2.55	0.27	1.009	0.052	94.0%	0.317	0.116	0.282	0.061
ang20151218t110045	Interface	2.55	0.30	1.509	0.067	95.0%	0.265	0.101	0.193	0.157
ang20151219t080745	Rural	2.42	0.33	0.523	0.055	89.0%	0.152	0.085	0.084	0.000
ang20151219t081738	Mixed	2.48	0.30	0.545	0.052	90.0%	0.147	0.071	0.193	0.001
ang20151219t082648	Mixed	2.47	0.36	0.596	0.073	87.4%	0.142	0.095	0.040	0.133
ang20151219t083640	Mixed	2.40	0.31	0.578	0.059	89.4%	0.160	0.074	0.009	0.029
ang20151219t084554	Interface	2.44	0.31	0.586	0.056	89.9%	0.161	0.096	0.062	0.011
ang20151219t090522	Mixed	2.12	0.23	0.540	0.050	90.3%	0.120	0.074	0.000	0.212
ang20151219t091521	Mixed	2.18	0.22	0.566	0.041	92.3%	0.130	0.060	0.016	0.055
ang20151219t092432	Mixed	2.19	0.22	0.617	0.043	92.8%	0.104	0.054	0.004	0.051
ang20151219t093417	Mixed	2.14	0.22	0.571	0.047	91.6%	0.189	0.105	0.067	0.005
ang20151219t100816	Mixed	3.13	0.33	1.373	0.051	95.7%	0.278	0.118	0.054	0.029
ang20151219t102124	Mixed	3.06	0.38	1.499	0.074	94.3%	0.628	0.346	0.456	0.280
ang20151221t074416	Agriculture	3.10	0.45	0.964	0.076	90.5%	0.537	0.329	0.231	0.117
ang20151221t075709	Agriculture	3.23	0.47	0.964	0.081	90.3%	0.572	0.237	0.058	0.000
ang20151221t081709	Agriculture	3.19	0.45	1.000	0.070	91.9%	0.493	0.191	0.044	0.013
ang20151221t082836	Mixed	3.21	0.47	0.981	0.061	92.8%	0.268	0.089	0.029	0.099
ang20160101t060341	Forest	1.50	0.07	0.257	0.192	25.2%	0.070	0.007	0.000	0.055
ang20160102t055138	Forest	1.50	0.05	0.209	0.158	19.7%	0.024	0.000	0.227	0.000
ang20160105t051247	Forest	1.50	0.04	0.298	0.273	8.8%	0.062	0.009	0.001	0.008
ang20160107t053300	Forest	2.19	0.24	0.415	0.086	79.4%	0.288	0.158	0.119	0.247
ang20160110t053216	Mixed	2.77	0.37	0.677	0.075	88.6%	0.172	0.078	0.119	0.012
ang20160126t053344	Agriculture	3.19	0.56	0.784	0.065	91.2%	0.230	0.056	0.597	0.132
ang20160127t075428	Agriculture	2.19	0.33	0.463	0.050	88.6%	0.117	0.044	0.032	0.035
ang20160127t090913	Agriculture	1.98	0.25	0.369	0.040	88.9%	0.087	0.062	0.101	0.045
ang20160128t050943	Fallow	2.36	0.40	0.571	0.050	90.5%	0.090	0.048	0.000	0.067
ang20160223t060914	Urban	1.00	0.20	0.141	0.052	64.0%	2.715	0.022	0.048	0.455
ang20160303t051027	Urban	2.88	0.62	0.681	0.082	87.7%	0.427	0.101	0.375	0.051
ang20160303t054522	Urban	2.84	0.61	0.587	0.084	85.7%	0.388	0.113	0.130	0.018

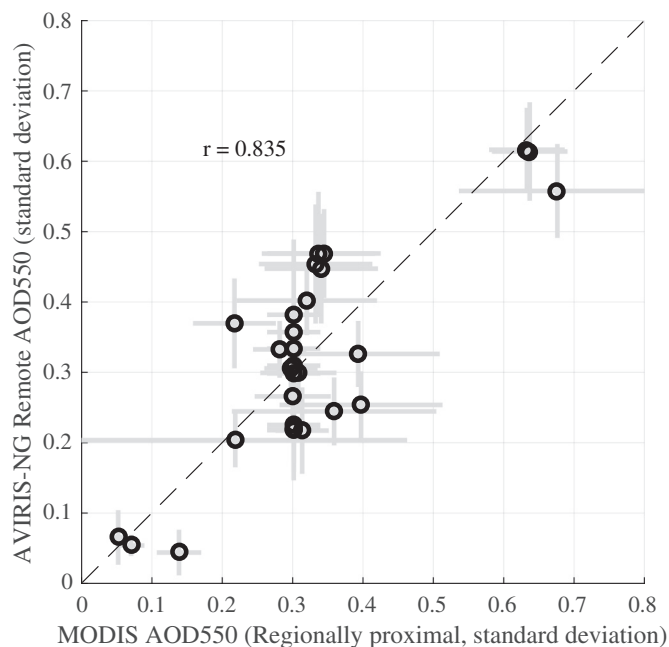


Fig. 17. Remote and AOD550 estimates from AVIRIS-NG and MODIS. Error bars show 1σ predicted uncertainties. MODIS observations are not spatio-temporally coincident. We create these mean estimates and standard deviations from observations on the same day acquired within a 1 degree latitude/longitude window. The correlation coefficient is $r = 0.835$.

retrievals directly as physical descriptions of aerosol particles. The retrievals imply some sensitivity to particle type, and a similar estimation approach might someday yield useful products for atmospheric science.

However, this will require considerable study. Validating retrievals would require a larger dataset of temporally-coincident in situ or AERONET measurements.

Another fruitful area for future work is the combination of retrievals at multiple spatial locations to infer smooth atmospheric fields. Factorizations using probabilistic approaches might tie the atmospheric parameters of nearby locations, allowing them to share information spatially and recover a global Maximum A Posteriori estimate (Thompson et al., 2018c). Efficient fixed-point approximations of this global solution could likely achieve near-optimality at reasonable computational cost.

Many factors in the observation conditions influence the ability to retrieve aerosols accurately. Surfaces at or near the Critical Surface Albedo (CSA) are independent of aerosol optical depth; this value changes depending on aerosol optical properties as well as the observing geometry (Seidel and Popp, 2012). For the purposes of recognizing distortions in atmospheric gas absorption features, it also depends on ambient water vapor abundance. In general, retrievals based on H₂O (or any other) absorption feature use darker portions of the spectrum, which generally improves the sensitivity for scattering aerosol while reducing it for absorbing aerosols. The rich interplay between surface albedo and aerosol optical properties highlights the benefit of multi-spectrum retrievals over varied land cover types in an image to achieve more accurate and physically interpretable aerosol estimates.

In summary, simulations, field validation experiments, and tests on large historical catalogs, demonstrate Optimal Estimation's value for improving surface reflectance retrievals under difficult atmospheric conditions. The method significantly outperforms conventional sequential approaches for a wide range of surfaces. It improves the accuracy of surface reflectances, as quantified by matches to field validation spectra and residual quality metrics. It also improves the consistency of atmospheric retrievals, while reducing interference from

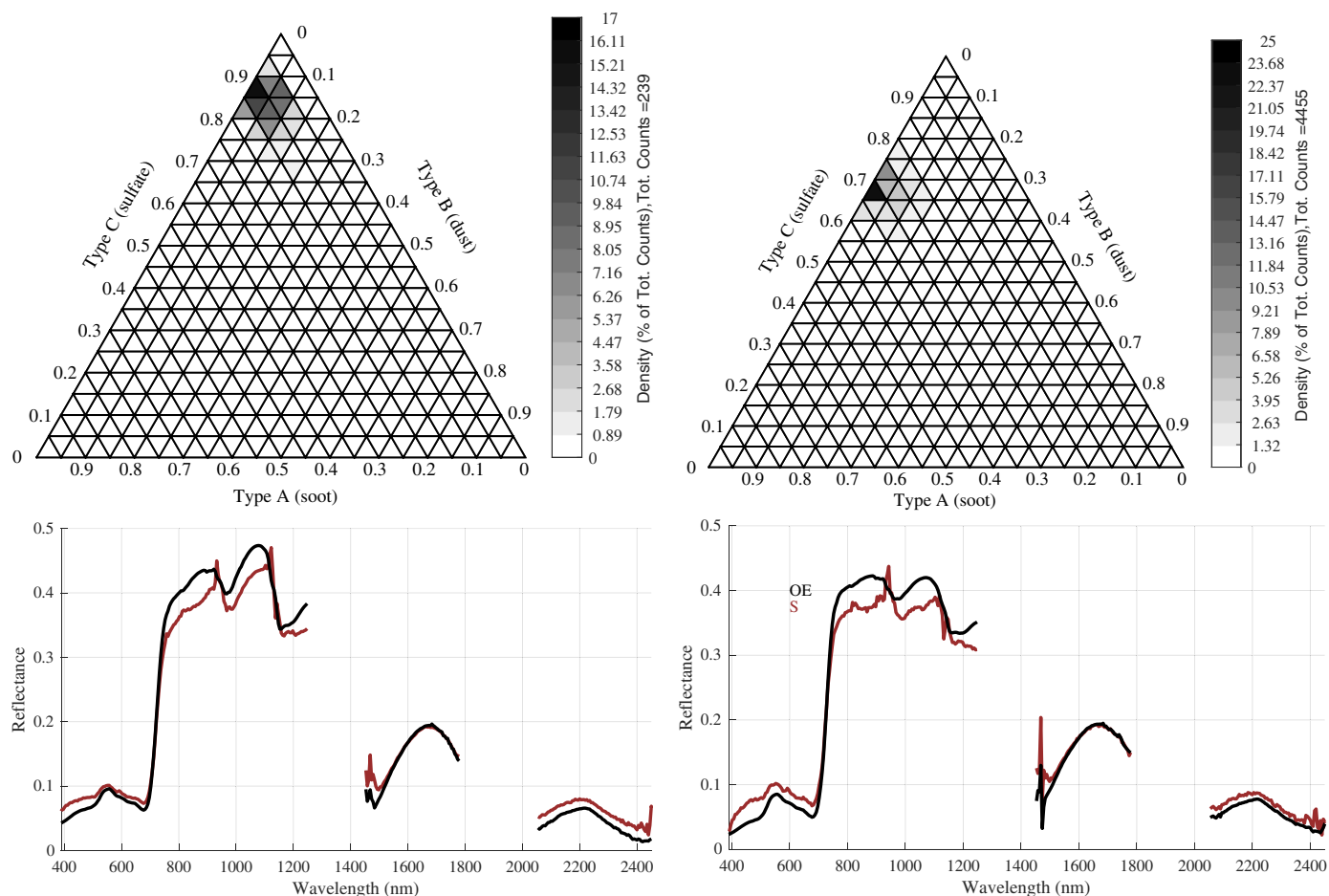


Fig. 18. Normalized AOD fractions for high-NDVI pixels from the first and last flightlines. Small differences in the proportion of aerosol type signatures show demonstrably different distortions in vegetation spectra. Red and Black lines show the AVIRIS-NG standard product result and Optimal Estimation retrievals, respectively. See text for explanation. (For interpretation of the references to colour in this figure legend, the reader is referred to the web version of this article.)

surface reflectance properties like liquid water absorption. Critically, it permits principled retrieval of aerosol properties simultaneously with surface and atmosphere, drawing information from the entire spectral range. This is sufficient for good quality reflectance retrieval, though the absolute accuracy of aerosol optical property retrievals requires further validation. Stronger prior information on aerosol types, derived from climatology or near-coincident direct observations, may provide better absolute AOD and property accuracy. An alternative for studies looking directly at aerosols would be to use a more specific surface model, such as the reflectance “basemap” (Thompson et al., 2018c) or a location-sensitive prior, providing very strong constraints on the surface reflectance for accurate aerosol distortion estimates. The ability for the designer to trade certainty in aerosols for surface reflectance, or vice versa, allows the same algorithm framework to be used for both objectives. These advantages make Optimal Estimation a compelling tool for atmosphere and surface retrievals in global VSWIR imaging spectroscopy missions.

Acknowledgment

We thank Sven Geier, Scott Nolte, and the AVIRIS-NG instrument

Appendix A. Aerosol climatology

We defined priors for the three aerosol type profiles by first identifying historical aerosol measurements on the Indian subcontinent, and then matching these optical properties using the aerosol types in the retrieval. The flights define a set of four climatologically and geographically distinct regions (Table A.6). We combined Level 2.0 data from the AEROSOL RObotic NETwork (AERONET) (Holben et al., 1998) at locations given in Table

and Science Data System teams for assistance in calibration and operations. Particular thanks go to Charles E. Miller. Bo-Cai Gao and Kevin Turpie provided important advice and tutelage. We are also thankful for the counsel of Phil Dennison, Dar Roberts, Steven Adler-Golden, and Alexander Berk. Rahul Nigam and Arundhati Misra also provided invaluable assistance during the AVIRIS-NG India campaign. We thank Dr. B. K. Bhattacharya for his oversight of the campaign. We acknowledge the support of the NASA Earth Science Division for the AVIRIS-NG instrument and the data analysis program “Utilization of Airborne Visible/Infrared Imaging Spectrometer Next Generation Data from an Airborne Campaign in India” NNH16ZDA001N-AVRNSG, managed by Woody Turner, for its support of the algorithm development. We are also thankful for the support of the Jet Propulsion Laboratory Research and Technology Development Program, and the NASA Center Innovation Fund managed in conjunction with the Jet Propulsion Laboratory Office of the Chief Scientist and Technologist. A portion of this research took place at the Jet Propulsion Laboratory, California Institute of Technology. Copyright 2019 California Institute of Technology. All Rights Reserved. US Government Support Acknowledged.

A.4. We used only the campaign timespan, the months from December through March, calculating average and standard deviations of the vertical total optical depth and single-scattering albedo. Determining the optical depths of the aerosol types which would match these distributions is tantamount to the problem of inferring the probability of specific aerosol optical depths τ for each aerosol type, given the AERONET observations, written $P(\tau_A, \tau_B, \tau_C | \tau_{AERONET}, SSA_{AERONET})$. We solve this by Monte Carlo integration over the PDF, drawing uniform samples from the distribution of $[\tau_A, \tau_B, \tau_C]$ described in Table A.5 below. We translate these to a total optical depth and single scattering albedo in each AERONET wavelength, and weighting the samples by the AERONET probability density. This produced prior means and standard deviations illustrated in Table A.6.

Table A.4
AERONET sites used to develop the aerosol climatology.

Site	Longitude	Latitude	Time Range
RM Nainital	79.458	29.359	2011–2012
Bareilly	79.437	28.390	2008
Bhola	90.750	22.167	2013–2015
Dhaka University	90.398	23.728	2012–2015
Gandhi College	84.128	25.871	2006–2017
Gual Pahari	77.150	28.426	2008–2010
IIT KGP EXT Kolkata	88.418	22.574	2009
Jaipur	75.806	26.906	2009–2016
Kanpur	80.232	26.513	2001–2017
Karachi	67.030	24.870	2006–2014
Kathmandu University	85.538	27.601	2009–2010
Lumbini	83.280	27.490	2013–2014
New Delhi	77.175	28.630	2009
Pune	73.805	18.537	2008–2016

Table A.5
Aerosol types A, B, and C are defined by scattering coefficients b_{sca} , absorption coefficients b_{abs} , and asymmetry parameters a .

nm	Type A			Type B			Type C		
	b_{abs}	b_{sca}	a	b_{abs}	b_{sca}	a	b_{abs}	b_{sca}	a
0.35	1.8391	1.30516	0.42162	0.94842	0.30727	0.8845	1.46048	0	0.7915
0.4	1.55629	1.14103	0.3951	0.95625	0.26111	0.85364	1.38796	0	0.79994
0.45	1.3324	1.00577	0.37188	0.99889	0.20303	0.81806	1.26332	0	0.79898
0.5	1.15307	0.89343	0.35124	1.00992	0.18524	0.80336	1.12755	0	0.79224
0.55	1	0.79195	0.33357	1	0.13374	0.77345	1	0	0.78405
0.6	0.88138	0.71293	0.31658	1.06295	0.11655	0.76158	0.881	0	0.77258
0.65	0.78987	0.65208	0.3	1.07499	0.11179	0.75224	0.77434	0	0.76052
0.7	0.70724	0.59389	0.28541	1.07951	0.10077	0.74054	0.67877	0	0.74672
0.75	0.64333	0.54921	0.27093	1.09373	0.09657	0.7334	0.59691	0	0.73218
0.8	0.58901	0.51033	0.25723	1.11003	0.09293	0.72755	0.52369	0	0.71686
0.9	0.5071	0.45095	0.23111	1.14892	0.08706	0.7207	0.40759	0	0.68601
1	0.4435	0.40185	0.20834	1.19154	0.08171	0.71769	0.31774	0.00001	0.65199
1.25	0.33926	0.31884	0.15821	1.31666	0.07877	0.72091	0.17826	0.00006	0.56602
1.5	0.27489	0.26381	0.11889	1.3459	0.07666	0.72387	0.10263	0.00017	0.4765
1.75	0.23505	0.22845	0.09029	1.41198	0.07507	0.73009	0.06293	0.00026	0.37145
2	0.20405	0.19999	0.06994	1.45288	0.07787	0.73425	0.04133	0.00137	0.28568
2.5	0.16286	0.1611	0.04517	1.27444	0.0943	0.74201	0.01637	0.00202	0.17831

Table A.6
Aerosol types A, B, and C are defined by scattering coefficients b_{sca} , absorption coefficients b_{abs} , and asymmetry parameters a .

Area	Latitude range	Longitude range	Type A prior τ_{550} (σ)	Type B prior τ_{550} (σ)	Type C prior τ_{550} (σ)
0	> 30° N	–	0.074 (0.134)	0.120 (0.079)	0.435 (0.10)
1	< 30°, ≥ 18° N	< 80° E	0.039 (0.10)	0.107 (0.276)	0.332 (0.115)
2	< 30°, ≥ 18° N	≥ 80° E	0.070 (0.141)	0.106 (0.075)	0.537 (0.10)
3	< 18° N	–	0.068 (0.10)	0.10 (0.070)	0.296 (0.149)

References

Asner, G., Martin, R., Knapp, D., Tupayachi, R., Anderson, C., Sinca, F., Vaughn, N., Llacayo, W., 2017. Airborne laser-guided imaging spectroscopy to map forest trait diversity and guide conservation. *Science* 355, 385–389.

Babu, S.S., Manoj, M.R., Moorthy, K.K., Gogoi, M.M., Nair, V.S., Kompalli, S.K., Satheesh, S.K., Niranjan, K., Ramagopal, K., Bhuyan, P.K., Singh, D., 2013. Trends in aerosol optical depth over indian region: potential causes and impact indicators. *Journal of Geophysical Research: Atmospheres* 118, 11,794–11,806.

Babu, K.N., Mathur, A.K., Thompson, D.R., Green, R.O., Patel, P.N., Prajapati, R.P., Bue, B.D., Geier, S., Eastwood, M.L., Helmlinger, M.C., 2019. An empirical comparison of calibration and validation methodologies for airborne imaging spectroscopy. *Current Science* 116 (7), 1101–1107.

Bedard, M., 2008. Optimal acceptance rates for metropolis algorithms: moving beyond 0.234. *Stoch. Process. Appl.* 118, 2198–2222.

Berk, A., Conforti, P., Kennett, R., Perkins, T., Hawes, F., van den Bosch, J., 2014. Modtran® 6: A Major Upgrade of the Modtran® Radiative Transfer Code. pp. 1–4.

Bernstein, L., Adler-Golden, S., Sundberg, R., Levine, R., Perkins, T., Berk, A., Ratkowski, A., Felde, G., Hoke, M., 2005. Validation of the quick atmospheric correction (QUAC)

- algorithm for VNIR-SWIR multi-and hyperspectral imagery. *Defense and Security* 668–678.
- Conel, J.E., Green, R., Vane, G., Bruegge, C., Alley, R., 1987. Ais-2 radiometry and a comparison of methods for the recovery of ground reflectance. In: *Proceedings of the 3rd Airborne Imaging Spectrometer Data Analysis Workshop*. vols. 87–30. pp. 18–47.
- Cressie, N., 2018. Mission CO2ntrol: a statistical scientist's role in remote sensing of atmospheric carbon dioxide. *J. Am. Stat. Assoc.* 113, 152–168.
- Dennison, P.E., Roberts, D.A., 2003. The effects of vegetation phenology on endmember selection and species mapping in southern California chaparral. *Remote Sens. Environ.* 295–309.
- Dubovik, O., Holben, B., Eck, T.F., Smirnov, A., Kaufman, Y.J., King, M.D., Tanré, D., Slutsker, I., 2002. Variability of absorption and optical properties of key aerosol types observed in worldwide locations. *J. Atmos. Sci.* 590–608.
- Dubovik, O., Herman, M., Holdak, A., Lapyonok, T., Tanré, D., Deuzé, J.L., Ducos, F., Sinyuk, A., Lopatin, A., 2011. Statistically optimized inversion algorithm for enhanced retrieval of aerosol properties from spectral multi-angle polarimetric satellite observations. *Atmospheric Measurement Techniques* 975–1018.
- Dubovik, O., Lapyonok, T., Litvinov, P., Herman, M., Fuertes, D., Ducos, F., Lopatin, A., Chaikovsky, A., Torres, B., Derimian, Y., et al., 2014. GRASP: a versatile algorithm for characterizing the atmosphere. *SPIE Newsroom*. <https://doi.org/10.1117/2.1201408.005558>.
- Dudley, K.L., Dennison, P.E., Roth, K.L., Roberts, D.A., Coates, A.R., 2015. A multi-temporal spectral library approach for mapping vegetation species across spatial and temporal phenological gradients. *Remote Sens. Environ.* 121–134 (Special Issue on the Hyperspectral Infrared Imager (HyspIRI)).
- Elvidge, C.D., 1990. Fresh and dry spectra of several plant tissues and chemical and phenological constituents (data set). In: *Ecological Spectral Information System (EcoSIS)*, (Last access: 19 Sept. 2018).
- ESAS, 2018. *Thriving on our Changing Planet: A Decadal Strategy for Earth Observation from Space. A Report by the Decadal Survey on Earth Science and Applications from Space*. The National Academies Press. Available online at, Washington, DC. <http://sites.nationalacademies.org/DEPS/esas2017/index.htm>, Accessed date: January 2018.
- Fichot, C.G., Downing, B.D., Bergamaschi, B.A., Windham-Myers, L., Marvin-DiPasquale, M., Thompson, D.R., Gierach, M.M., 2015. High-resolution remote sensing of water quality in the San Francisco Bay–Delta estuary. *Environ. Sci. Tech.* 573–583.
- Frankenberg, P.U.C., Wagner, T., 2005. Retrieval of CO from SCIAMACHY onboard ENVISAT: detection of strongly polluted areas and seasonal patterns in global CO abundances. *Atmos. Chem. Phys.* 1639–1644.
- Friedl, M.A., Sulla-Menashe, D., Tan, B., Schneider, A., Ramankutty, N., Sibley, A., Huang, X., 2010. Modis collection 5 global land cover: algorithm refinements and characterization of new datasets. *Remote Sens. Environ.* 168–182.
- Gao, B.C., Goetz, A.F., 1990. Column atmospheric water vapor and vegetation liquid water retrievals from airborne imaging spectrometer data. *Journal of Geophysical Research: Atmospheres* 95, 3549–3564.
- Gao, B.-C., Kaufman, Y.J., 2003. Water vapor retrievals using moderate resolution imaging Spectroradiometer (MODIS) near-infrared channels. *Journal of Geophysical Research: Atmospheres* 108.
- Gao, B.C., Heidebrecht, K.B., Goetz, A.F., 1993. Derivation of scaled surface reflectances from AVIRIS data. *Remote Sens. Environ.* 165–178.
- Gao, B.-C., Montes, M.J., Davis, C.O., Goetz, A.F., 2009. Atmospheric correction algorithms for hyperspectral remote sensing data of land and ocean. *Remote Sens. Environ.* S17 – S24 (Imaging Spectroscopy Special Issue).
- Gelman, A., Shirley, K., et al., 2011. Inference from simulations and monitoring convergence. In: *Handbook of Markov Chain Monte Carlo*. vol. 6. pp. 163–174.
- Gilks, W.R., Richardson, S., Spiegelhalter, D.J. (Eds.), 1996. *Markov Chain Monte Carlo in Practice*. Chapman and Hall, London.
- Guanter, L., Gómez-Chova, L., Moreno, J., 2008. Coupled Retrieval of Aerosol Optical Thickness, Columnar Water Vapor and Surface Reflectance Maps from ENVISAT/MERIS Data over Land.
- Guanter, L., Kaufmann, H., Segl, K., Foerster, S., Rogass, C., Chabrilat, S., Kuester, T., Hollstein, A., Rossner, G., Chlebek, C., et al., 2015. The EnMAP spaceborne imaging spectroscopy mission for earth observation. *Remote Sens.* 8830–8857.
- Higurashi, A., Nakajima, T., 1999. Development of a two-channel aerosol retrieval algorithm on a global scale using noaa avhrr. *J. Atmos. Sci.* 924–941.
- Hobbs, J., Braverman, A., Cressie, N., Granat, R., Gunson, M., 2017. Simulation-based uncertainty quantification for estimating atmospheric CO₂ from satellite data. *SIAM/ASA Journal on Uncertainty Quantification* 5, 956–985.
- Hochberg, E.J., 2011. Remote sensing of coral reef processes. In: *Coral Reefs: An Ecosystem in Transition*, pp. 25–35.
- Holben, B.N., Eck, T.F., Slutsker, I., Tanre, D., Buis, J., Setzer, A., Vermote, E., Reagan, J.A., Kaufman, Y., Nakajima, T., et al., 1998. Aeronet-a federated instrument network and data archive for aerosol characterization. *Remote Sens. Environ.* 1–16.
- Hou, W., Wang, J., Xu, X., Reid, J.S., Han, D., 2016. An algorithm for hyperspectral remote sensing of aerosols: 1. Development of theoretical framework. *J. Quant. Spectrosc. Radiat. Transf.* 178, 400–415.
- Hou, W., Wang, J., Xu, X., Reid, J.S., 2017. An algorithm for hyperspectral remote sensing of aerosols: 2. Information content analysis for aerosol parameters and principal components of surface spectra. *J. Quant. Spectrosc. Radiat. Transf.* 192, 14–29.
- Iwasaki, A., Ohgi, N., Tani, J., Kawashima, T., Inada, H., 2011. Hyperspectral imager suite (HISUD)-japanese hyper-multi spectral radiometer. In: *Proceedings of the 2011 IEEE International Geoscience and Remote Sensing Symposium (IGARSS)*, pp. 1025–1028.
- Jetz, W., Cavender-Bares, J., Pavlick, R., Schimel, D., Davis, F.W., Asner, G.P., Guralnick, R., Kattge, J., Latimer, A.M., Moorcroft, P., Schaeppman, M.E., 2016. Monitoring plant functional diversity from space. *Nat. Plants* 2 (3), 16024.
- Keshava, N., Mustard, J.F., 2002. Spectral unmixing. *IEEE Signal Process. Mag.* 44–57.
- King, M.D., Menzel, W.P., Kaufman, Y.J., Tanré, D., Gao, B.-C., Plattnick, S., Ackerman, S.A., Remer, L.A., Pincus, R., Hubanks, P.A., 2003. Cloud and aerosol properties, precipitable water, and profiles of temperature and water vapor from modis. *IEEE Trans. Geosci. Remote Sens.* 41, 442–458.
- Kuhlmann, G., Hueni, A., Damm, A., Brunner, D., 2016. An algorithm for in-flight spectral calibration of imaging spectrometers. *Remote Sens.* 1017.
- Labate, D., Ceccherini, M., Cisbani, A., De Cosmo, V., Galeazzi, C., Giunti, L., Melozzi, M., Pieraccini, S., Stagi, M., 2009. The PRISMA payload optomechanical design, a high performance instrument for a new hyperspectral mission. *Acta Astronautica* 1429–1436.
- Lawson, C., Hanson, R., 1995. *Solving Least Squares Problems*. Society for Industrial and Applied Mathematics, Philadelphia.
- Levy, R., Mattoo, S., Munchak, L., Remer, L., Sayer, A., Patadia, F., Hsu, N., 2013. The collection 6 modis aerosol products over land and ocean. *Atmospheric Measurement Techniques* 2989.
- Lin, C.-I., Baker, M., Charlson, R.J., 1973. Absorption coefficient of atmospheric aerosol: a method for measurement. *Appl. Opt.* 1356–1363.
- Lyapustin, A.I., Wang, Y., Laszlo, I., Hilker, T., Hall, F.G., Sellers, P.J., Tucker, C.J., Korkin, S.V., 2012. Multi-angle implementation of atmospheric correction for modis (MaiaC): 3. Atmospheric correction. *Remote Sens. Environ.* 385–393.
- Perkins, T., Adler-Golden, S., Matthew, M., Berk, A., Bernstein, L., Lee, J., et al., 2012. Speed and accuracy improvements in FLAASH atmospheric correction of hyperspectral imagery. *Optical Engineering* 111707–111707–7.
- Reinersman, P.N., Carder, K., Chen, R., 1998. Satellite-sensor calibration verification with the cloud-shadow method. *Appl. Opt.* 5541–5549.
- Richter, R., Schläpfer, D., 2002. Geo-atmospheric processing of airborne imaging spectrometry data, part 2: atmospheric/topographic correction. *Int. J. Remote Sens.* 23, 2631–2649.
- Ripley, B.D., 1987. *Stochastic Simulation*. Wiley, New York.
- Roberts, D.A., Gardner, M., Church, R., Ustin, S., Scheer, G., Green, R., 1998. Mapping chaparral in the Santa Monica mountains using multiple endmember spectral mixture models. *Remote Sens. Environ.* 267–279.
- Rodgers, C.D., 1976. Retrieval of atmospheric temperature and composition from remote measurements of thermal radiation. *Reviews in Geophysics and Space Physics* 14, 609–624.
- Rodgers, C.D., 1990. Characterization and error analysis of profiles retrieved from remote sounding measurements. *J. Geophys. Res.* 5587–5595.
- Rodgers, C.D., 1996. Information content and optimisation of high spectral resolution measurements. In: *Proceedings of the SPIE*.
- Rodgers, C.D., 2000. *Inverse Methods for Atmospheric Sounding: Theory and Practice*. pp. 2.
- Schaepman, M.E., Ustin, S.L., Plaza, A.J., Painter, T.H., Verrelst, J., Liang, S., 2009. Earth system science related imaging spectroscopy—an assessment. *Remote Sens. Environ.* S123–S137.
- Schläpfer, D., Hueni, A., R., 2018. Cast shadow detection to quantify the aerosol optical thickness for atmospheric correction of high spectral resolution optical imagery. *Remote Sens.* 25.
- Seidel, F.C., Popp, C., 2012. Critical surface albedo and its implications to aerosol remote sensing. *Atmospheric Measurement Techniques* 1653–1665.
- Serbin, S., DuBois, S., Jablonski, A., Desai, A., Kruger, E., Townsend, P., 2018. Nasa HyspIRI California Airborne Campaign Ground Target Spectra (Data Set). *Ecological Spectral Information System (EcoSIS)* (Last access: 19 Sept. 2018).
- Teillet, P., Fedosejevs, G., 1995. On the dark target approach to atmospheric correction of remotely sensed data. *Can. J. Remote Sens.* 374–387.
- Theiler, J., 2012. The incredible shrinking covariance estimator. In: *SPIE Defense, Security, and Sensing*. International Society for Optics and Photonics, pp. 83910P.
- Thompson, D.R., Gao, B.-C., Green, R.O., Roberts, D.A., Dennison, P.E., Lundein, S.R., 2015. Atmospheric correction for global mapping spectroscopy: ATREM advances for the HyspIRI preparatory campaign. *Remote Sens. Environ.* 64–77.
- Thompson, D.R., Boardman, J.W., Eastwood, M.L., Green, R.O., Haag, J.M., Mouroulis, P., Gorp, B.V., 2018a. Imaging spectrometer stray spectral response: in-flight characterization, correction, and validation. *Remote Sens. Environ.* 850–860.
- Thompson, D.R., Guanter, L., Berk, A., Gao, B.-C., Richter, R., Schläpfer, D., Thome, K.J., 2018b. Retrieval of Atmospheric Parameters and Surface Reflectance from Vswir Imaging Spectroscopy Data. *Surveys in Geophysics*.
- Thompson, D.R., Natraj, V., Green, R.O., Helmlinger, M., Gao, B.-C., Eastwood, M., 2018c. Optimal estimation for imaging spectrometer atmospheric correction. *Remote Sens. Environ.* 355–373.
- Thompson, D.R., Cawse-Nicholson, K., Erickson, Z., Fichot, C.G., Frankenberg, C., Gao, B.-C., Gierach, M.M., Green, R.O., Jensen, D., Natraj, V., Thompson, A., 2019. A unified approach to estimate land and water reflectances with uncertainties for coastal imaging spectroscopy. *Remote Sensing of Environment* 231, 111198 (in press). <https://doi.org/10.1016/j.rse.2019.05.017>.
- Ustin, S.L., Roberts, D.A., Gamon, J.A., Asner, G.P., Green, R.O., 2004. Using imaging spectroscopy to study ecosystem processes and properties. *BioScience* 54, 523–534.
- Verhoef, W., van der Tol, C., Middleton, E.M., 2017. Hyperspectral radiative transfer modeling to explore the combined retrieval of biophysical parameters and canopy fluorescence from FLEX - Sentinel-3 tandem mission multi-sensor data. *Remote Sens. Environ.* <https://doi.org/10.1016/j.rse.2017.08.006> (in press).
- Vermote, E.F., Kotchenova, S., 2008. Atmospheric correction for the monitoring of land surfaces. *Journal of Geophysical Research: Atmospheres* 113.
- Wang, M., Antoine, D., Frouin, R., Gordon, H.R., Fukushima, H., Morel, A., Nicolas, J.-M., Deschamps, P.-Y., 2010. In: Wang, M. (Ed.), *Reports of the International Ocean-Colour Coordinating Group, IOCCG Report 10: Atmospheric Correction for Remotely-Sensed Ocean-Colour Products*. MacNab Print, Dartmouth, Canada, pp. 23 chapter 4.

- Xu, F., van Harten, G., Diner, D.J., Kalashnikova, O.V., Seidel, F.C., Bruegge, C.J., Dubovik, O., 2017. Coupled retrieval of aerosol properties and land surface reflection using the airborne multiangle spectropolarimetric imager. *Journal of Geophysical Research: Atmospheres* 122, 7004–7026.
- Yoshida, Y., Ota, Y., Eguchi, N., Kikuchi, N., Nobuta, K., Tran, H., Morino, I., Yokota, T., 2011. Retrieval Algorithm for CO₂ and CH₄ Column Abundances from Short-Wavelength Infrared Spectral Observations by the Greenhouse Gases Observing Satellite.
- Zong, Y., Brown, S.W., Johnson, B.C., Lykke, K.R., Ohno, Y., 2006. Simple spectral stray light correction method for array spectroradiometers. *Appl. Opt.* 1111–1119.